JAAS

ROYAL SOCIETY OF CHEMISTRY

PAPER

Cite this: *J. Anal. At. Spectrom.*, 2026, **41**, 385

Tracing the *post-mortem* history of Egyptian mummies using nuclear microprobe analysis of trace metal elements and mineral dust particles

Didier Gourier, *[ab] Océane Anduze,[ab] Quentin Lemasson,[bc] Laurent Pichon,[bc] Thomas Calligaro,[bc] Agnès Lattuati-Derieux[ba] and Laurent Binet[ab]

Received 1st September 2025
Accepted 12th November 2025

DOI: 10.1039/d5ja00339c

rsc.li/jaas

Trace metal elements present in black matter coatings and airborne dust particles trapped by Egyptian mummies were studied by combining μ-PIXE and μ-IBIL spectroscopy and mapping. Among the samples from 16 mummies that were analyzed, a detailed study was carried out on fragments of strips and black matter detached from the enigmatic human mummy preserved in the *Musée de Boulogne-sur-Mer*, France. Quantification of V and Ni showed that the mummy's bitumen comes from an unknown source, different from the Dead Sea which was the main source of bitumen in the black matter of the other studied mummies. Abundant microparticles of Egyptian blue pigment and of airborne aluminosilicate and carbonate particles trapped on both sides of the samples were detected by μ-PIXE and μ-IBIL, with more aluminosilicates on the inner side of strips, facing the mummy, and more carbonates on the outer faces, facing outward. The nature and distribution of dust particles suggested that the mummy was exposed to at least two dust events: one event in South Egypt during preparation of the mummy, and the other in Northern Egypt after excavation of the mummy. The abundance of mercury indicates that the mummy had undergone, in the first third of the 19th century, undocumented treatments with mercury salts to protect the mummy against insects and fungi.

Introduction

Many mummies discovered during ancient excavations of Egyptian necropolises, carried out in the first half of the 19th century, are now on display in museums after spending time in private collectors' cabinets. In many cases, little is known about these mummies, as writings about them have been lost, or are suspect, or do not exist. The mummy of an unknown man conserved in the *Musée de Boulogne-sur-Mer* (hereafter referred to as BSM), France, is a good illustration of this situation. Despite the limited information available on this mummy, it is of real historical interest for several reasons. Acquired in 1837 by the museum from a private Parisian collector, the mummy was contained in two nested coffins (the intermediate and outer coffins), while the inner coffin is conserved in the *Musée des Beaux-Arts*, Grenoble, France (Fig. S1). The outer coffin disappeared probably during the 1st world war. A 19th-century handwritten inscription on the inner coffin reads (in French):[1,2] "Mummy from the catacombs of Thebes (…) brought back by Vivant Denon from the French expedition, 1799", which refers to Napoleon Bonaparte's expedition in Egypt (Fig. S1). However, the author of this inscription is unknown, which casts doubt on the real origin of this funerary ensemble. Furthermore, it was suspected that the mummy was not the genuine occupant of these coffins, but was placed in them to improve their market value, a common practice in the 19th century.[3] Finally, it was this mummy that led Auguste Ferdinand Mariette, one of the fathers of Egyptology in the 19th century, to discover Ancient Egypt: "I entered Egypt (…) through the mummy in the Musée de Boulogne".[4] The coffins belong to Nehemsimontou, a priest from Thebes who probably lived in the 8th century BC, *i.e.* during the end of the XXVth dynasty.[5] The mummy's body is partially coated with a solid, black, shiny substance showing drips at some places (Fig. S2). Damaged by insect attacks, and badly weakened (right wrist and both ankles broken), this mummy was consolidated in 2004 at the Centre de Recherche et de Restauration des Musées de France (C2RMF) Paris, France.[6,7] During these interventions, fragments of strips covered with black matter became detached from the head and the neck and were conserved for later study.

Surprisingly, the analysis of these samples by Electron Paramagnetic Resonance (EPR) and gas chromatography coupled with single quadrupole mass spectrometry (GC-MS) revealed that the shiny black coating of the mummy consists of pure bitumen,[8] whereas analyses of embalming matter in

[a]PSL University, Chimie-ParisTech, CNRS, Institut de Recherche de Chimie-Paris (IRCP), F-75005 Paris, France. E-mail: didier.gourier@chimieparistech.psl.eu
[b]Centre de Recherche et de Restauration des Musées de France (C2RMF), Palais du Louvre, F-75001 Paris, France
[c]PSL University, Lab BC, CNRS, UAR 3506, C2RMF, Palais du Louvre, F-75001 Paris, France

Egyptian mummies generally show that they are made up of complex mixtures of different natural substances (vegetable resins, beeswax, fats, *etc.*),[9–15] with variable proportions of bitumen ranging from 0% to a maximum of 35–40%.[16–18] EPR provided highly sensitive and non-destructive method for detection and quantification of vanadyl porphyrins (VO–P) at trace levels, which are specific molecular markers of bituminous oil and bitumen.[19] In VO-Ps, VO^{2+} ions are coordinated with the four nitrogen atoms of the porphyrin rings, but in mummy coatings, these VO-P complexes are partially transformed into oxygen coordinated VO^{2+} complexes.[8,20] Surprisingly, the VO-Ps of the BSM mummy's bitumen showed no sign of chemical transformation, so that this apparent "freshness" of the bitumen coating could suggest that the mummy was embellished before it was sold with the coffins in the early 19th century, by covering it partially with pure bitumen. Consequently, two questions arise about this unaltered bitumen coating. The first one is its geographical origin, given that by far the most important source of bitumen in ancient Egypt was the Dead Sea.[11,16,21–25] The second one concerns the time when this bitumen was applied to the mummy, which may have been either during its mummification in ancient Egypt, or at the beginning of the 19th century to embellish and protect it from attack by insects and other organisms.

To address these questions and in order to obtain more information on this mummy, trace element heritage of the strips and the coating was used as a chemical memory of the *post-mortem* mummy's history, from its mummification to its exhibition in the museum. We can distinguish three potential generations of trace elements that could have marked the mummy's history. The first one is present in the black coating itself, with variable enrichment in V, Ni and S which can provide information on the source of the bitumen.[16,26–29] The second generation of trace elements belongs to mineral dust microparticles from the airborne fraction of soil and man-made materials, present in the ambient environment of mummification, and that have been trapped on the mummy during its preparation.[30,31] The third generation of trace elements appeared after the mummy has been excavated and displayed in a private collection or museum, where it may have undergone other dust input and more or less documented protective treatments during the 19th–20th centuries.

In general, the analysis of minerals is based on classical petrological methods, *i.e.* polarized light microscopy, scanning electron microscopy (SEM) and X-ray diffraction (XRD). Polarized light microscopy, however, requires the preparation of very thin slides. Apart from the fact that we have very few samples of the mummy, as the others were sacrificed in the GC/MS and EPR studies,[8,20] these fragments are extremely fragile and composite, and therefore highly unsuitable for the design of thin slides. SEM observation with X-ray secondary emission analysis (EDS analysis) is possible directly on a sample, but the latter must be placed under high vacuum (low vacuum in the case of environmental SEM), and it is necessary to make it conductive by treating the surface. These analytical methods must therefore be regarded as destructive for these rare, precious and fragile human remains. In the present work, major, minor and trace chemical elements present in the BSM mummy and other mummies were analyzed by combining μ-Particle Induced X-ray Emission (μ-PIXE), μ-Ion Beam Induced Luminescence (μ-IBIL), and proton Elastic Back Scattering (EBS).[32]

Materials and methods

Description of samples

During consolidation work on the BSM mummy in 2004 at the C2RMF, pieces of strips covered with black matter became detached from the neck and the head (Fig. 1), and were preserved for analysis.[7] Some pieces were analyzed visually during this intervention. Several fragments were sacrificed in 2019 for GC-MS, EPR and Hyperfine spectroscopy analyses.[8,20] Three other fragments were analyzed in the present work by combined PIXE-IBIL-EBS analysis. For these samples, labelled 1, 2 and 3, we distinguished their inner face α (facing the mummy) and the outer face β (facing outward). Sample 1 is a fragile fragment of strip, with one face soaked with brown, matt-looking black matter, and with the other face covered with smooth, shiny black matter showing drips, which indicates that it is the outer face β of the sample (Fig. 1b). Sample 2 is a very fragile strip fragment detached from the top of the head, with a clean outer face β, and the inner face α covered with a thick layer of black matter that partly extends over the outer face (Fig. 1c). Sample 3 is a monolithic and solid plate of black matter, with a dull brown inner face α, and the outer face β showing drips (Fig. 1d). This face was not analyzed for reasons of limited beam time.

Two other series of samples of embalming matter (labelled corpus A and corpus B) were taken from 15 different mummies, and were analyzed by PIXE and IBIL for comparison with the BSM mummy. These samples have been previously described and analyzed in detail by EPR and PIXE for some metallic elements (Ni, V and Mo).[16] Their characteristics are summarized in Table S1. They belong to 9 birds (labelled 1 to 14) for corpus A, and 2 rams (An1 and An2/An3), 1 crocodile (An4), 1 human mummy (Hum2) and a fragment of black matter taken from the bottom of a human coffin (Hum1) for corpus B. Fragments of bitumen from the Dead Sea (DS) were also used as a reference.

The external proton beam analysis system

Combined μ-PIXE, μ-IBIL and μ-EBS analyses of raw samples were carried out in air at the AGLAE facility (Accelerateur Grand Louvre pour l'Analyse Elémentaire) of the C2RMF located in the *Palais du Louvre*, Paris. In this system, a 3 MeV external proton micro-beam with ≈ 30/40 μm diameter scanned the sample surface with a fast vertical magnetic deflection of the beam as a 40×500 μm^2 brush across a 100 nm thick Si_3N_4 exit window, as it was slowly mechanically translated. PIXE spectra were collected with four 50 mm^2 SDD-EDX detectors (Ketek AXAS-A), with one low energy (LE) and three high energy (HE) detectors, positioned at 45° and 50°, respectively, relative to the beam axis (Fig. S3). The HE detectors were covered with a 100 μm Mylar filter to collect X-rays from minor and trace elements ($Z > 20$). The LE detector was fitted with a magnetic deflector under a 1

L min^{-1} He flow and was used to record X-rays of light elements ($10 < Z < 29$), which can reveal the presence of mineral dust microparticles embedded in the black organic coatings and the linen strips. The simultaneous combination of three HE detectors is equivalent to a high solid angle super detector, increasing significantly the detection limit for trace elements without increasing irradiation doses.[33] The optical luminescence (μ-IBIL) was collected with a 1 mm diameter optical fibre placed at 3 mm distance of the sample and at 45°, and was conducted to a research grade OCEAN OPTICS QE65000 spectrometer recording from 200 to 1000 nm with a resolution of 3 nm FWHM.[34] The elastically backscattered protons (EBS) for detection of major elements of the organic matter (C, N, O) were collected by a PIPS detector (Passivated Implanted Planar Silicon) at 135° with respect to the incident beam (Fig. S3).

The small size and fragility of the samples (Fig. 1) required precautions to preserve their integrity during measurement. However, the spatial pixel size of 25 μm enabled us to map a minimum area of 500 × 500 μm^2, on sample sizes of the order of 10 mm. To analyze such small samples, they were placed on a support topped by a plastiline cylinder covered with plastic film, so as to raise their surface vertically and perpendicular to the beam axis, while avoiding any contamination of the samples.[16] The areas mapped on each sample were pre-selected from binocular loupe images of both sides of the three samples. The selection criteria were (i) a fairly flat surface, as large as possible (several mm^2 ideally), which would be the subject of large-scale mapping (over 2000 × 2000 μm^2) in the first instance (ii) various visible surface heterogeneities, concentrated in a single region of interest (ROI) which would be the subject of smaller-scale targeted mapping (500 × 500 μm^2 to 1000 × 1000 μm^2) in the second instance. Once the samples have been placed on the support, the camera of the beamline end station was used to pinpoint the areas selected for analysis. The different zones mapped are represented in Fig. 1, and the analytical procedure is described in SI Section S2.3. The different mappings are labelled as follows, taking $3\alpha_1$ and $1\beta_4$ as examples: the 1st digit is the sample number (1, 2, 3); the Greek letter represents the face of the sample (α for inner and β for outer); the last number in index is the mapping number, which makes it easy to identify the mappings carried out on each sample. The characteristics of the various mappings carried out in this work, namely total and effective numbers of pixels per mapping, proton dose collected in μC, beam intensity in nA, and beam fluence in μC cm^{-2}, are given in Table S2. More details on the selection and analysis of the maps are given in Section S2.2 of the SI.

Data processing for μ-PIXE, μ-IBIL and μ-EBS analyses

The interaction of the 3 MeV proton beam with the bitumen coating was modelled using *Stopping and Range of Ions in Matter* (SRIM 2008) software, which calculates the effects of ion interaction with matter.[35] These calculations give a path length of 127 μm for protons in pure bitumen with a density of 1.1 g cm^{-3}. So, if a linen strip is covered with a layer of bitumen of thickness d, the proton beam will only probe the bitumen if $d > \approx 130$ μm. It will probe both the bitumen and the strip if the bitumen layer is much thinner. Also, the decay of proton energy as it penetrates the material (bitumen or strip) has a dual impact on embedded mineral dust analysis. Firstly, the efficiency of PIXE emission decreases as protons no longer have the nominal energy (3 MeV), and secondly, the X-rays emitted at depth are attenuated as they travel towards the detector. These

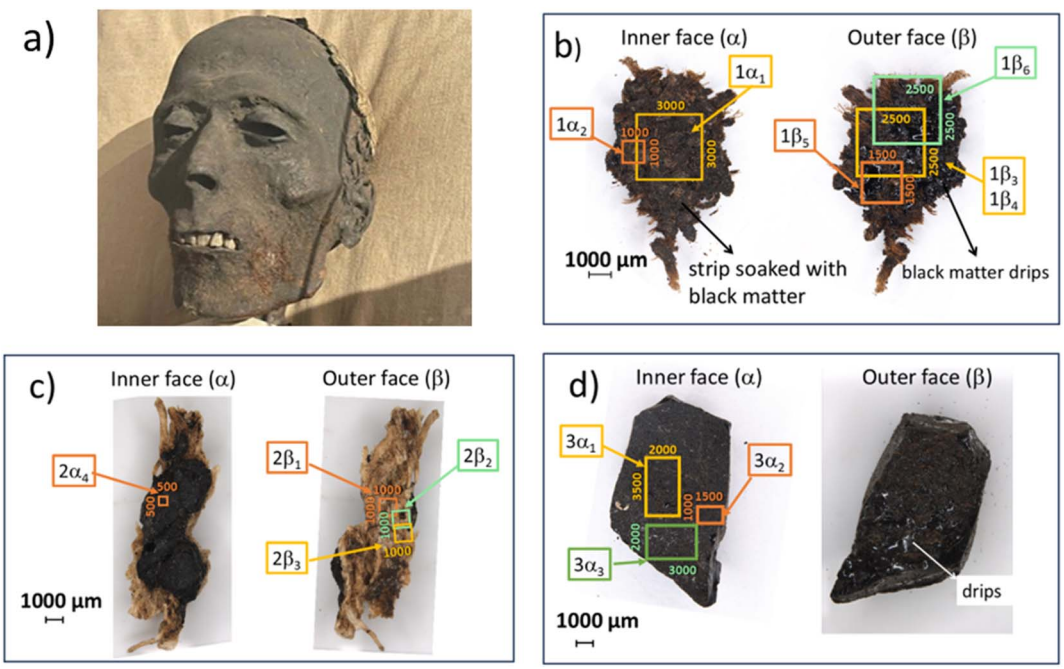

Fig. 1 (a) Head of the BSM mummy (Boulogne-sur-Mer Museum collection, inv.1a.R2) © Didier Gourier; (b–d) photographs of the two faces (inner side α, and outer side β) of samples 1, 2 and 3 taken from the head and neck © O.Anduze; the area mapped by the proton beam are represented by coloured squares and rectangles.

two combined effects have a strong impact on the quantification of light elements, primarily Al and Si.[36] A simulation of this burial effect is given in Table S3 for Ca/Al, Si/Al and Ca/Fe ratios. Qualitative information on the depth of localization of mineral particles is provided by IBIL. The visible or near infrared (NIR) light emitted by buried particles is strongly absorbed by the highly absorbent overlying material (bitumen or linen strip), and only the light emitted by surface particles can be collected.

For each mapped area (homogeneous zone or mineral dust), the μ-PIXE, μ-IBIL and μ-EBS spectra collected are the sums of the spectra for each pixel on that area (see Table S2). Qualitative analysis of the mapped areas was carried out using *AGLAEMap*,[37] an in-house software package that simultaneously displays and analyzes all the data acquired during a single run (LE- and HE-PIXE, IBIL, EBS). The principle behind the qualitative comparison of PIXE and IBIL data using *AGLAEMAP* is described in Section S2.2 of the SI, and an example of IBIL analysis is described in Fig. S4.

PIXE data were processed using the *GUPIX* software,[38] coupled to the in-house *TRAUPIXE* software for quantifying the chemical elements that make up the bituminous matrix and those that may indicate chemical contamination.[37] All the PIXE spectra were simulated taking into account 44 elements from Na to U. Analyses of homogeneous zones and dust micro-grains were carried out by toggling back and forth between *GUPIX* and the open source *PyMca* software.[39] In all cases, sum spectra recorded from the LE and HE detectors were combined in one unique PIXE spectrum by using pivot elements, which are present in both spectra in the range 3–10 keV.[37] For the complex and composite mummy fragments, whose chemical composition is inherently difficult to analyze, we chose two pivot elements (Ca and Fe) for more rigorous quantification. EBS data were simulated by the *SIMNRA* software.[40] Once the experimental set-up is defined, the target (sample plus the thin gaseous layer of helium/air) is described as a succession of layers with, for each layer, its thickness and the relative atomic concentration of elements.

Results and discussion

Light elements

As all the samples consist mainly of materials of biological origin such as linen fibers, organic embalming materials including bitumen and other possible biological compounds (skin, feathers …), the elements C, N and O are expected to be the most abundant. However, these light elements are not accessible by PIXE while they are easily detected by elastic backscattering of incident protons (EBS). Instead of resulting from coulombic repulsion of protons by nuclei (Rutherford Back Scattering, RBS), which predominates for heavy elements (high nuclear charge), the elastic scattering by light elements (low nuclear charge) is mainly due to nuclear reactions following the penetration of the proton into the nucleus. The corresponding non-Rutherford backscattering cross-sections of C, N, O are approximately ten times higher than their Rutherford counterpart. Fig. 2 shows a comparison of the sum μ-EBS spectra of selected area of solid bitumen (DS sample) and of a sample covered with a thick layer of black matter ($2\alpha_4$ mapping). The μ-EBS spectrum of pure bitumen (Fig. 2a) shows that it contains almost exclusively C, with O and S in smaller proportions. The narrow He and N peaks are due to the thin gaseous layer of helium and air between the sample surface and the proton beam exit window. The *SIMNRA* simulation, which also took into account the presence of hydrogen, gives the values C (73 wt%), H (12 wt%), O (6 wt%) and S (9 wt%). The same EBS spectrum was obtained on BSM samples covered with black matter, as shown in Fig. 2b for $2\alpha_4$ mapping. This resemblance with the EBS spectrum of pure bitumen is in good agreement with the EPR and GC-MS analyses of the black matter samples of the BSM mummy, which showed them to be composed of pure bitumen.[8,20] It can be noted that the oxygen content of bitumen in the mummy is twice that of DS bitumen, as shown by comparing the simulations of EBS spectra (Fig. 2). The spectrum of $2\alpha_4$ mapping also shows a very weak backscattered proton signal extending towards high energies, beyond 2650 keV (dotted circle on the inset of Fig. 2b), whereas this signal does not appear in the reference bitumen (DS). These differences indicate the presence of heavier elements, that can be explained if the bitumen of the mummy sample is partially covered by fine mineral dust, mostly oxides (which partially contribute to the increase of O/C) which also contain heavier metallic elements (EBS signal extending to higher energies than S threshold). These chemical elements are not transition elements such as Fe, V and Ni, which are also fairly abundant in

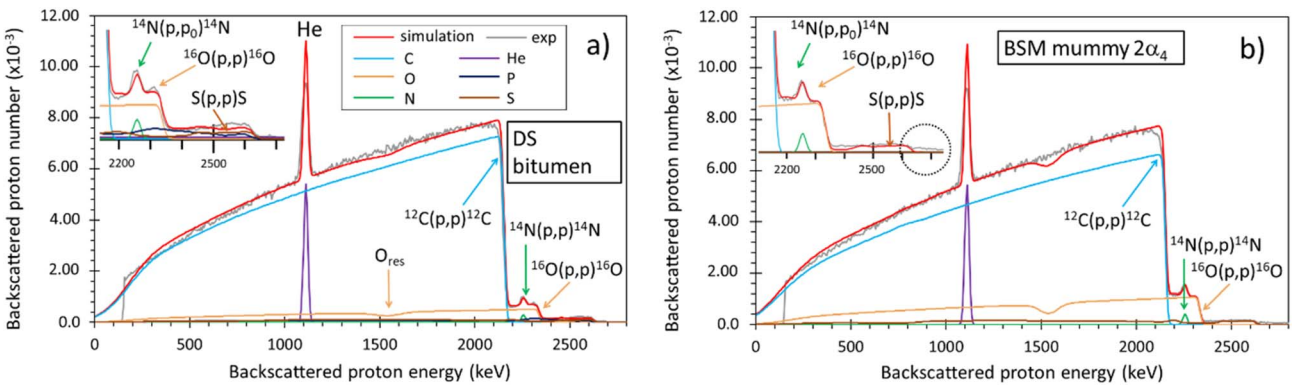

Fig. 2 Experimental (grey noisy lines) and simulated (red lines) EBS spectra of the BSM mummy; (a) pure Dead Sea bitumen, (b) the black layer of sample 2 ($2\alpha_4$ mapping); the different components of the simulations are represented by colored lines.

bitumen, but more probably Hg and Pb whose presence will be clearly demonstrated by the following PIXE analyses. The fact that the carbon signal remains very intense shows that the surface of the BSM sample is only partially covered with mineral dust, otherwise this signal would decrease considerably in the case of a completely covered surface.

Identification and sourcing of bitumen by V and Ni trace elements

V and Ni enrichment in oil and bitumen, in the form of vanadyl and nickel porphyrins, is a specific marker of these fossil hydrocarbons.[28,29] Recently, the Ni/V ratio has been used to identify the Dead Sea region as the most likely source of the bitumen present in the embalming materials of several ensembles of human and animal mummies.[16,41] When the source of the bitumen is identified from the Ni/V ratio and absolute V content, it is then possible to estimate the proportion of bitumen present in the embalming materials.[16] Fig. 3 shows two examples of experimental and simulated sum μ-PIXE spectra recorded on homogeneous areas of the two faces of sample 2 of the BSM mummy, with indication of X-ray emission peaks of chemical markers of bitumen (V, Ni, S), of mineral dust particles (Al, Si, Ca, Fe), and of heavy elements (Hg, Pb) discussed in the next sections. Two pivot elements (Ca and Fe) were used for constructing the total PIXE spectrum from LE and HE detectors. The other PIXE spectra and the corresponding concentrations of several elements discussed in this work are given in Fig. S5 and Tables S4–S8.

Information on the bitumen present in the BSM mummy were deduced from the V, Ni and S contents measured from the μ-PIXE sum spectra recorded in homogeneous zones of the samples. The fact that these three chemical elements are excellent markers for bitumen is well illustrated by the PIXE spectra of sample 2 (Fig. 3a, b and Table S4), which show almost no V, Ni and S on the outer surface 2β displaying only clean linen fibers, and high levels of V, Ni and S on the inner surface 2α covered with a thick layer of black matter. As bitumen is always more or less enriched in S, its quantity is roughly proportional to the amount of bitumen probed by the proton beam. Fig. 3c shows the variation in V + Ni content as a function of S content for all mappings carried out on the three BSM

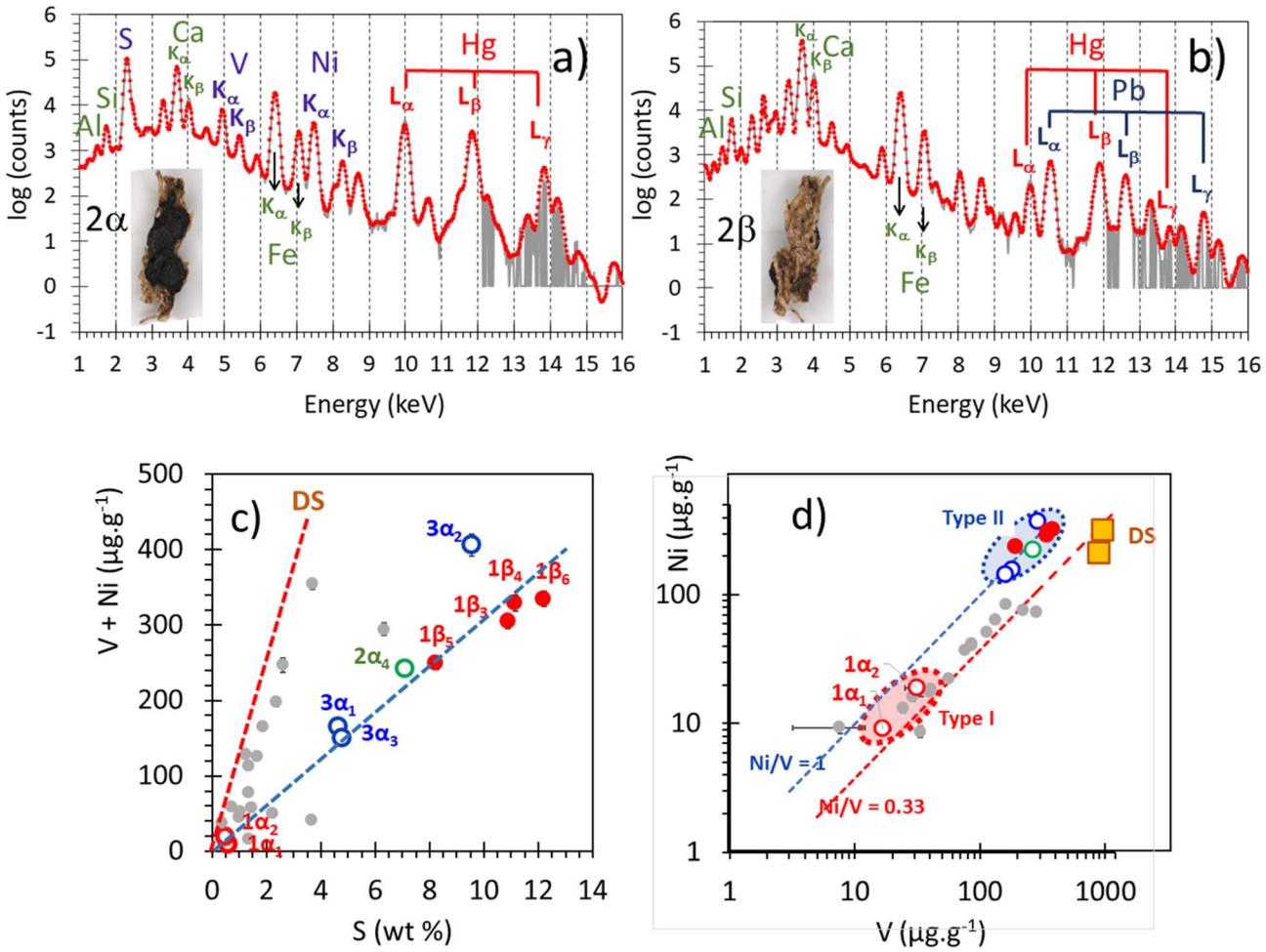

Fig. 3 (a) and (b) experimental (grey lines) and simulated (red points) sum μ-PIXE spectra of $2\alpha_4$ and $2\beta_2$ mappings in the BSM mummy; (c) V + Ni contents *versus* S contents, and (d) Ni contents *versus* V contents measured on homogeneous zones of samples in the BSM mummy (red, green and blue circles), and in birds, rams, crocodile and human mummies of corpus A and B (light grey circles); data bor DS bitumen are represented by yellow squares.

mummy samples (red, blue and green circles), and those previously recorded from birds, rams, crocodile and human mummies in corpus A and B (light grey circles).[16] The dashed red line is the one measured for bitumen originating from the Dead Sea (DS). The nearly linear relationships between V + Ni and S contents in almost all mummies (Fig. 3c) show that these elements are components of the bitumen fraction of the samples. Most of the data in corpus A and B are close to the DS line, confirming that their embalming matters contain variable amounts of DS bitumen.[16] Some data points are far from this line, but these samples are bird feathers, which contain notable quantities of sulphur present in keratin. The experimental points for the BSM mummy are clearly different from those of mummies in corpus A and B, and are placed on a line with a smaller slope than the DS line (dashed blue line), indicating that the bitumen of the BSM mummy contains fewer metallic elements and more sulphur than DS bitumen. Sample 1 of the BSM mummy, which is a fragment of linen strip covered on both sides with a layer of black matter, shows a peculiar behavior (Fig. 3c). Its outer surface 1β (full red circles), which contains a significant quantity of V, Ni and S, is compatible with a black matter composed exclusively of bitumen, as previously shown by EPR and GC-MS.[8] In contrast, the inner surface 1α (open red circles), which has the same visual aspect as the outer face, contains very little V, Ni and S, indicating that this thin layer of black matter contains very little bitumen (Fig. 3c and d). In particular, Fig. 3d highlights two interesting features. The first is that the data points $1\alpha_1$ and $1\alpha_2$ of the inner face of sample 1 contain very little Ni and V with a ratio Ni/V ≈ 0.5–0.6 close to the ratio 0.3–0.5 measured for the DS bitumen of mummies in corpus A and B.[16] This black matter will be hereafter referred to as black matter of type I (Fig. 3d). As the V content of DS bitumen is about 900–1000 μg g^{-1}, and that of the 1α surface is only 20–30 μg g^{-1}, this indicates that the black matter of type I contains only 2–3% of DS bitumen. The second interesting feature is that all the 7 other experimental points for the BSM mummy (1β, 2α, 3α mappings, colored circles) have a much higher V and Ni content, with Ni/V ≈ 0.85 to 1.3, different from the values Ni/V ≈ 0.3 to 0.5 measured for mummies containing DS bitumen.[16] As EPR and GC-MS analyses have shown that the black matter in the BSM mummy is mainly composed of pure bitumen,[8] it is therefore a bitumen with Ni/V close to 1, with the same amount of nickel than DS bitumen, but with 2 to 3 times less vanadium. This pure bitumen layer will be referred to as black matter of type II (Fig. 3d).

It has been shown that Ni/V < 0.5 values are characteristic of an anoxic marine origin of the source sediments of oil/bitumen, while Ni/V in the range $1 \leq$ Ni/V ≤ 10 is characteristic of a lacustrine or terrestrial origin.[26] Therefore, the source of bitumen predominantly used for the BSM mummy (Type II) is clearly not the Dead Sea. Two oil families are present in the Gulf of Suez (Red Sea).[42] Family 1, to which Dead Sea bitumen also belongs, has a Ni/V lower than 0.5 and a S content much larger than 1%, and was derived from sulphur and metal-rich kerogen source rocks deposited in an anoxic hypersaline marine environment. Family 2, to which bitumen from the oil leaks of the Gebel El Zeit region (southern Gulf of Suez) also belongs, has a lower metal content and a higher Ni/V ratio, close to 0.9, and derived from a mixed marine-continental origin.[42] The bitumen used for the BSM mummy (type II), with its Ni/V ratio between 0.9 and 1.3, is compatible with this family 2. In support of this hypothesis, it has been shown by GC-MS that the bitumen used for the mummy of Pasenhor (western Thebes) could have come from natural oil leaks at Jebel El Zeit.[22] However, such a source is not assured for the BSM mummy, since family 2 is characterized by a S content of less than 1%, whereas it can reach 12% in the bitumen from the BSM mummy. There would therefore appear to be an incompatibility between the high sulphur content that characterizes source rocks of anoxic marine origin, and the high Ni/V ratio and the low V content that characterizes source rocks of continental or lacustrine origin. Given this uncertainty about a local source (Egypt or Dead Sea) for the bitumen of the BSM mummy, more distant sources can also be considered, such as Mesopotamia. Indeed, bitumen found at an archaeological site (Sakheri Sughir) near the ancient cities of Ur and Eridu in today's southern Iraq, has a Ni, V contents and Ni/V ratio identical to those measured for the BSM mummy.[43] As these sites are located near the Euphrates, the bitumen could originate from the Hit region upstream, which was an important source of bitumen in Mesopotamia in ancient times.[23,44] However, although the high sulfur content of Hit bitumen (7 to 12 wt%) is compatible with that of BSM mummy, its Ni/V ratio (0.2 to 0.3) is too low.[45] We must therefore admit that the source for the bitumen from the BSM mummy remains unknown.

In summary, the present μ-PIXE analysis revealed that two types of embalming matter would have been used for the BSM mummy. A first coating (type I), probably consisting of the same type of mixture usually employed for embalming in Ancient Egypt (resins, beeswax, *etc.*) with 2–3% of Dead Sea bitumen, would have been applied at first, but this very discrete coating is scarcely present in the detached fragments of the mummy. The mummy was then partially or totally covered with layers of pure bitumen of unknown origin (type II). Although we do not have any indication of the precise anatomic location of the samples detached from the mummy's neck and head, a close look at a photograph taken during the mummy's restoration in 2004 (Fig. S2) already seems to support these observations. It shows the presence of smooth, shiny black material, in brittle patches detached from the neck, and applied on top of matt, brownish material. While the matt brown matter appears to cover the entire face and neck of the deceased, the shiny black materials applied above are clearly visible on the neck. It is also very abundant on many other parts of the mummy.[6,7]

It remains to be investigated whether this upper shiny black and chemically unaltered bitumen layer was due to an intervention in the early 19th century, consisting of a partial or total treatment of the mummy with fresh bitumen in order to embellish/protect it. Attempting to determine when and where this layer of pure bitumen was applied – during the mummification process in ancient Egypt, or in the early 19th century – is the object of the following sections dealing with trapped mineral dust particles.

Mineral particles from airborne dust

About 40% of the global aerosols in the troposphere are mineral dust particles produced by wind erosion on arid surface, with a major contribution from different sources in North Africa.[46] With sizes ranges from about 0.1 μm to more than 20 μm, these particles are composed of a variety of minerals among which quartz, clays, feldspars, calcite, iron oxides, with relative abundances depending on the source origin.[46–48] Other minerals with a more local origin are those synthesized by man in ancient Egypt, such as pigments. Fine particles of all these types of minerals may be present in the ambient atmosphere of mummification sites and may have been trapped in the strips and mummy's coating. Therefore, their identification and localization in the samples are likely to provide information about the *post-mortem* mummy's history.

Regarding the μ-PIXE/μ-IBIL analysis, we may distinguish two types of particles according to their size. The largest ones, with size larger than the pixel size (about 25 μm) appear as spots in μ-PIXE and (or) μ-IBIL mappings. The presence of particles much smaller than the pixel size particles can only be deduced from the sum μ-PIXE spectra in mappings of apparently homogeneous areas of samples. Concerning the depth of trapping in the material (bitumen or linen strip) of a particular type of mineral dust emitting both in PIXE and IBIL, we will distinguish between particles trapped on the surface, characterized by a detected luminescence and whose quantification of light elements (Al, Si, …) is unaffected by attenuation effects, and buried particles, whose optical luminescence is reabsorbed by the overlying material and is not detected, and whose quantification of light elements is progressively altered as depth increases.[36]

Global mineralogical composition of trapped dust. Aluminum is an ideal marker of mineral dust (MD) because it is absent in biological matter (skin, fats, linen, resin, wax, …) and in bitumen. As Al contributes to about 8% to the composition of the continental crust,[49] the weight% of mineral dust trapped by the mummy samples can be roughly estimated by MD = Al/0.08. Based on the average Al concentration measured on all the mappings (Table S6), we can estimate that the BSM samples contain about 6 wt% of mineral dust, with twice as much dust on their inner sample surfaces α ($MD_\alpha \approx 8$ wt%) than their outer surfaces β ($MD_\beta \approx 4$ wt%).

Al and Ca contents mostly reflect the presence of aluminosilicates and carbonates dust trapped on the mummy. It appears that contrary to Al which is more abundant on the inner surfaces α, Ca is more abundant on the outer surfaces β (0.7 to 1.7 wt%) than on the inner surfaces α (0.3 to 0.7 wt%) of the samples. This indicates that there is more aluminosilicates and less calcium carbonates below the strips (*i.e.* facing the mummy), and more calcium carbonates and fewer aluminosilicates above the strips (*i.e.* facing outwards). This asymmetry in the dust distribution is well illustrated in Ca/Al and (Ca + Mg)/Fe ratios (Fig. 4a), which both represent the relative contents of carbonates and aluminosilicates, and have been used as markers of airborne dust sources in North Africa.[46,47] The Ca/Al and (Ca + Mg)/Fe markers play the same role, as they are correlated for a given population of dust,[47] but the latter would be more influenced by the variability of Fe content, which is sensitive to anthropic contamination and possible traces of blood in the case of mummies. A recent analysis of airborne dust from Egypt and Tunisia suggested three types of sources, based on Ca/Al ratio:[47] (i) sand dunes (erg-like sources), with Ca/Al < 2; (ii) saline playas (chotts-like sources), with Ca/Al > 6, and (iii) limestone surfaces for the intermediate values 2 < Ca/Al < 6, which may also correspond to a mixture of dust from erg-like and chott-like sources. The broad dispersion of Ca/Al values in the BSM mummy (Fig. 4a) suggests different sources and episodes of dust input, which is not too much surprising owing to the long *post-mortem* history of the mummy, and considering also the preparation of the mummy took place over ∼70 days,[50] whereas the residence time of airborne dust in the troposphere does not exceed 10 days.[51] However, we can observe that the inner sample surfaces 1α and 3α have Ca/Al in the range 0.3 to 1.5, which correspond to an erg-like source of dust (Ca/Al < 2). On the other hand, the outer sample surfaces 1β and 2β are more dispersed and characterized by higher Ca/Al values 2 < Ca/Al < 11, which correspond to those measured for dust originating from the calcareous plateau and saline basins of northwestern Egypt.[47] Remarkably, the experimental points reported in the Ca/Al *versus* (Ca + Mg)/Fe diagram (Fig. 4a) for the BSM mummy match with the three types of dust sources defined by Boraly *et al.*[47] represented by colored areas in Fig. 4a, except for the inner surface 3α. This anomaly of 3α mappings is not due to an excess of magnesium-rich minerals (dolomite, olivine, magnesite), because their Mg content (200–600 μg g^{-1}) is lower than that of 1α mappings (1000–1600 μg g^{-1}) (Table S6). It is rather due to a Fe deficit in 3α compared to 1α, as shown on Fig. 4b representing Ti *versus* Fe concentrations. Fe is sensitive to anthropogenic contamination, while Ti is exclusively associated with minerals of natural origin,[46] with an average ratio Ti/Fe = 0.1 for the continental crust (dashed line in Fig. 4b).[49] Consequently, values Ti/Fe < 0.1 would correspond to an excess of Fe, which may indicate a modern anthropic pollution of trapped dust particles, while Ti/Fe > 0.1 indicates an excess of Ti. Overall, the dust trapped on animal and human mummies from corpus A and B (light grey circles in Fig. 4b) has Ti/Fe values that globally agree with a continental crust origin. Regarding the BSM mummy, all the mappings give Ti/Fe ≥ 0.1, which rule out the presence of blood or any modern anthropic Fe pollution of the samples. The "anomalous" mappings 3α shows a lower Fe content than 1α, and has a Ti enrichment factor EF ≈ 3 with respect to the continental crust ($EF = (Ti/Fe)_{sample}/(Ti/Fe)_{crust}$). EF is lower for mappings 1α (EF ≈ 1.4) and 1β (EF ≈ 2), while 2β mappings exhibit a pure continental crust composition (EF = 1). The excess of Ti with respect to Fe is likely due to an enrichment in Ti-rich minerals, which is a known characteristic of airborne dust from Sahara.[52] Therefore, an enrichment in Ti can be considered as another signature of an erg-like source. This is also the case of bird's mummies 4, 11 and 12, which have the highest mineral contents of corpus A and B, and also show a significant Ti excess (EF = 2, 1.7 and 2.7, respectively).

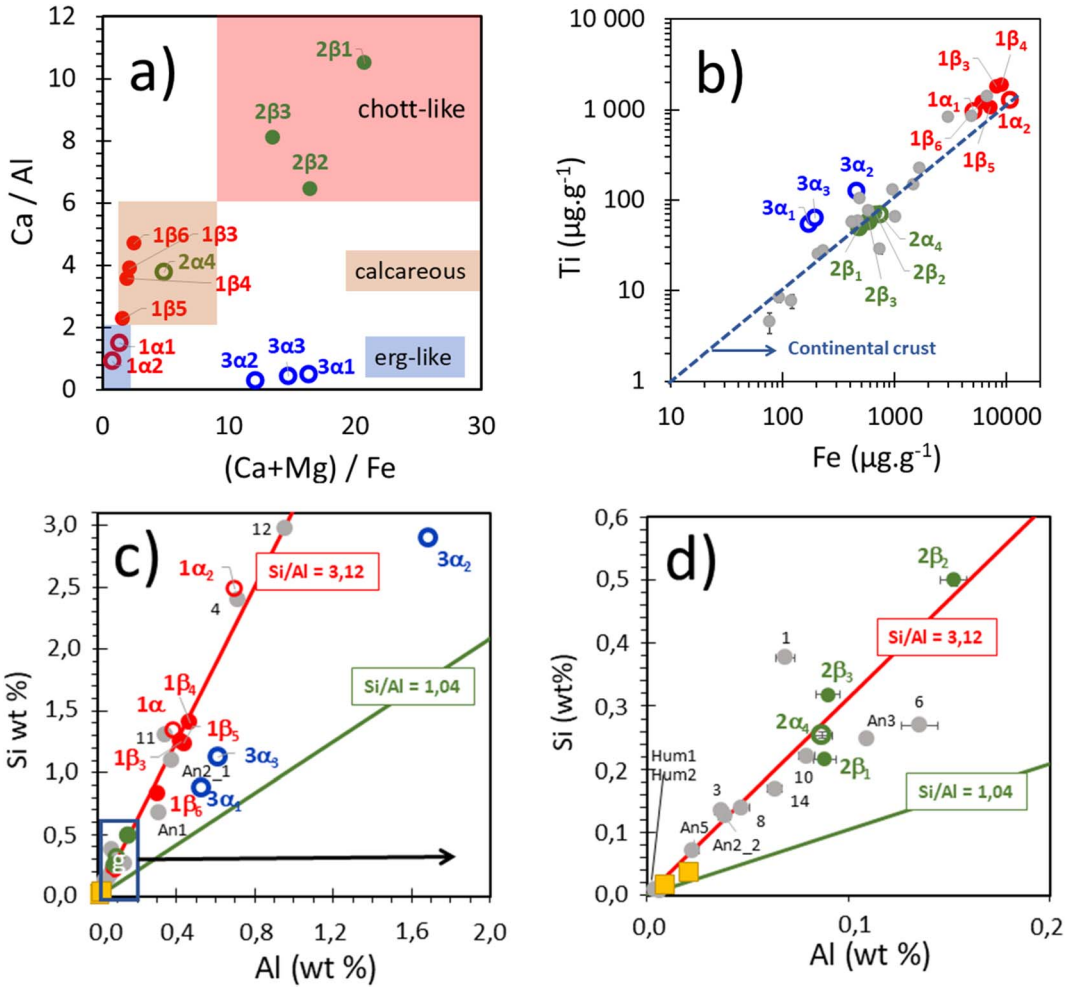

Fig. 4 Ca, Al, Si, Ti and Fe content of the mummies, measured on homogeneous zones of samples; (a) Ca/Al *versus* (Ca + Mg)/Fe for the BSM mummy; the colored areas correspond to the three types of dust sources defined by Boraly *et al.*;[47] (b) Ti content *versus* Fe content; the dashed blue line corresponds to the continental crust composition; (c) Si contents *versus* Al contents for the BSM mummy, and for samples from corpus A and B; (d) zoom of the lower left part of diagram (c); the straight lines correspond to theoretical variations for alkaline feldspars (red line) and for minerals such as anorthite or kaolinite (green line); data for the BSM mummy are represented by colored circles, and data for corpus A et B are represented by light grey circles; the yellow squares are data for DS bitumen.

It is important to note that the diagram in Fig. 4a only makes sense if the dust particles are located on the surface of the samples. Indeed, the quantification of light elements, Al and Si in particular, is strongly affected by the depth at which the dust particles are located within the material.[36] The Ca/Al ratio increases sharply with depth, while the Ca/Fe ratio decreases slightly (Table S3). We have seen that the Ca/Al and (Ca + Mg)/Fe ≈ Ca/Fe ratios for the 2β mappings correspond well to known ratios for chott-like dusts (Fig. 4a), but this is only true if these mineral particles are on the surface of the samples. Indeed, let us suppose these particles are located, for instance, 30 µm below the surface, in which case the measured values $(Ca/Al)_{exp}$ = 8 to 10 and $(Ca/Fe)_{exp}$ ≈ 0.8 to 1 would correspond to real values $(Ca/Al)_{real}$ = 0.6 to 1, and $(Ca/Fe)_{real}$ ≈ 14 to 23 for these mineral particles, which does not correspond to any type of dust in North Africa.[46,47] As a consequence, the good correspondence between the ratios measured for the BSM mummy and the dust categories defined by Boraly *et al.*,[47] indicates that the particles are trapped on the surface of the samples. This is also demonstrated below in the case of aluminosilicates.

From this analysis, we can propose the hypothesis that several dust events may have occurred during the *post-mortem* history of the BSM mummy: (i) a first dust event from an erg-like source (Ca/Al < 2 and EF > 1) which occurred before application of the bitumen coating and wrapping of the mummy (inner faces α); (ii) other dust events dominated by chott-like sources (6 < Ca/Al < 11, EF ≈ 1) and calcareous sources (2 < Ca/Al < 6) took place after the mummy was covered with its bandages (outer faces β). In Egypt, the strongest winds, called Khamaseen, blow from west to east and are more frequent in spring (March to May). They carry huge clouds of Saharan dust over great distances, and are characterized by Ca/Al < 2 and EF > 1.[47,52] On the contrary, Ca/Al ratios of aerosols are found to be larger and more variable during moderate dust events, which occur with the regular winds blowing most of the year in Egypt from the north-west to the north-east.[47] In this case, the dust has

a regional origin and comes from the erosion of soils in the West Nile desert, whose geology is dominated by limestones plateaus dating from the Eocene to the Miocene,[53] but also includes depressions (Qattara, Siwa, Fayum, Farafra …), whose bottoms are covered with a mixture of salts and sands, responsible for the highest Ca/Al values.

In this model, mummification would have taken place in spring, during which an episode of Khamaseen would have deposited Saharan dust on the mummy before the application of the bitumen and the wrapping. At least another dust input, richer in carbonates (calcite) and salts (gypsum), would have occurred after the bandaging of the mummy, either at the end of the mummy's preparation and before its burial, or after its exhumation in the 19th century. It is not easy to decide between these two options. However, Ca/Al < 2 values are characteristic of aerosols in southern Egypt and Sudan, while higher values are found in northern Egypt.[46] In this case, the Khamaseen episode would have taken place during mummification in the Thebes region, where the mummy is supposed to have come from, while the second dust episode would have taken place in northern Egypt at the beginning of the 19th century, *i.e.* after the coffins had been excavated and opened, and the mummy prepared for shipment to France.

Interestingly, the fact that abundant Saharan dust could have settled on the body during its mummification indicates that the embalming workshop was probably ventilated (open temporary building or tent), which is understandable given the need to evacuate gases emitted by the putrefying body.[54]

Nature and localization of aluminosilicate dust. The Si and Al elements closely reflect the presence of silicate and aluminosilicate dust trapped on the mummy, since these chemical elements are very seldom found in bitumen (Fig. 4d and Table S5) and in biological matter. After oxygen, Si and Al are the most abundant elements in the continental crust, with a mean value Si/Al ≈ 3.4. For this reason, Si and Al are very abundant in dust and sediments from northern Africa, with Si/Al ratio in the range 2.5 to 7 depending on the abundance of quartz SiO_2.[46] The apparent Si and Al contents measured on homogeneous areas of samples from the BSM mummy and the mummies of corpus A (birds) and B (rams, crocodile, human) are given in Fig. 4c, with Fig. 4d being a zoom for the low content part of the diagram. The corresponding values are reported in Table S6. The red and green lines represent boundary atomic ratios Si/Al = 3 and Si/Al = 1, corresponding to mass ratios 3.12 and 1.04, respectively. Feldspars are the most abundant minerals of the continental crust (about 60%). They form a solid solution between a calcic pole (anorthite $CaAl_2Si_2O_8$), corresponding to Si/Al = 1, and a sodic pole (albite $NaAlSi_3O_8$) with Si/Al = 3, constituting the plagioclase series, and another series between albite and the potassic pole (orthoclase, microcline and sanidine $KAlSi_3O_8$) constituting the alkali feldspar series with Si/Al = 3. However, it must be noted that an atomic ratio Si/Al = 3 is not exclusive to alkali feldspars, and is also found in other common granite minerals such as biotite $K(Mg,Fe)_3(OH, F)_2(Si_3AlO_{10})$ (black mica) for example. Similarly, an atomic ratio Si/Al = 1 is found in phyllosilicates present in aerosols, such as kaolinite $Al_2Si_2O_5(OH)_4$, a mineral derived from the alteration of feldspars, or also muscovite $KAl_2(AlSi_3O_{10})(OH,F)_2$, a white mica commonly found in granites and metamorphic rocks. So, the Si/Al ratio alone is not enough to identify the nature of aluminosilicate particles, and also because an apparent Si/Al = 3 ratio can just as easily correspond to a grain of alkali feldspar (Si/Al = 3) trapped on the surface, as to a grain of kaolinite (Si/Al = 1) trapped at a depth of 30 μm in the bitumen (Table S3). Hence the need to identify the nature of the mineral dust in order to assess its trapping depth.

Three preliminary observations can be made from the apparent Si/Al ratios reported in Fig. 4c and d: (i) the vast majority of studied mummy samples, whether human or animal, are characterized by $1 < Si/Al \leq 3$, indicating that quartz SiO_2 is only a very minor component of trapped dust; (ii) with the notable exception of the mappings 3α from the BSM mummy, with Si/Al ≈ 1.7–1.8 (3α mappings are also particular in Ca/Al *versus* (Ca + Mg)/Fe diagrams, see Fig. 4a), all the samples from this mummy and the bird mummies (corpus A) have Si/Al ratios very close to 3, indicating the predominance of a specific type of aluminosilicate dust at a specific depth, in all these samples; (iii) The high aluminosilicate content of inner surfaces $3\alpha_2$ and $1\alpha_2$, and to a lesser extent $1\alpha_1$, $3\alpha_1$ and $3\alpha_3$, are in good agreement with their low Ca/Al < 2 ratio, which classifies them as erg-like dust.

We can go further in the identification and localization of these abundant aluminosilicate dusts by examining their μ-IBIL spectra. These take the form of weakly emitting spots in the far red-NIR around 750–770 nm. Fig. 5a and b show two examples of luminescent particles observed in μ-IBIL mappings $1\beta_4$ and $1\beta_5$. Fig. 5d shows a similar spectrum recorded on an μ-IBIL mapping from a bird mummy (bird of prey) found in Giza (sample 8 of corpus A, see SI Section S1.2). This red-NIR emission around 750–770 nm is generally accompanied by a weaker green emission centred around 560–580 nm (Fig. 5). These two emission bands are attributed to Fe^{III} (750–770 nm) and Mn^{II} (560–580 nm) impurities in feldspar particles. Indeed, natural feldspars always contain atomic defects, including Fe^{III} impurities that substitute Al^{3+} in $[AlO_4]^{5-}$ units (Fig. S6c), which are responsible for the red luminescence of these minerals.[55–58] Feldspars can also exhibit other emission bands, such as a green band around 540–570 nm due to Mn^{II} impurities at the Ca^{2+} site, and a blue band around 420–500 nm attributed to intrinsic defects.[59] Both Fe^{III} and Mn^{II} have a d^5 electronic configuration, with their emissions being the $^4T_1 \rightarrow {}^6A_1$ spin forbidden transition in the weak crystal field regime (high-spin configuration) (see Fig. S6d). Several studies showed that Fe^{III} luminescence in feldspars varies in the range 690 nm to 770 nm, depending on the mineral composition.[58,60–62] Thus, the luminescence can provide additional information on the nature of the feldspars trapped on the mummy. The strength of the crystal field, which controls the energy of the optical transition, depends on the length of the Fe–O bond. The shorter the bond, the stronger the crystal field, and the lower the energy *E* of the emitted photons, and therefore the longer their wavelength (see Fig. S6d). The Fe^{III} luminescence wavelength is maximum for albite (around 750–770 nm) and decreases to ≈ 690 nm as the potassium content increases (alkali feldspar series) or as the

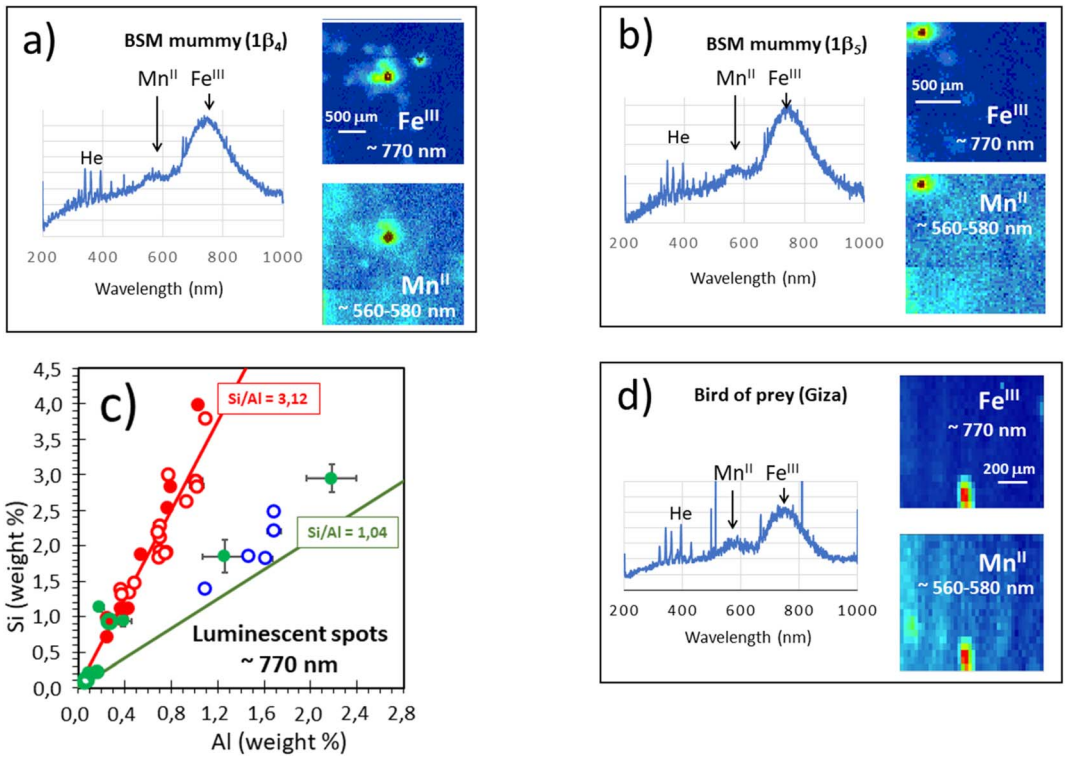

Fig. 5 Luminescence of albite microparticles; (a) and (b) µ-IBIL spectra and µ-IBIL mappings at ~770 nm and ~560–580 nm of $1\beta_4$ and $1\beta_5$ surfaces; (c) Si and Al contents of luminescent spots of sample 1 (red circles), sample 2 (green circles) and sample 3 (blue circles) of the BSM mummy; open circles and full circles correspond to the inner and outer faces, respectively; (d) µ-IBIL spectrum and µ-IBIL mappings at ~770 nm and ~560–580 nm of a bird of prey from Giza (sample 8 of corpus A); the very narrow peaks in the 400 nm region correspond to atomic emission lines of helium.

calcium content increases (plagioclase series).[62] In the case of the mummies we analysed, the emission band around 750–770 nm corresponds to that of albite. As this mineral may contain up to 10% of Ca, Mn^{II} impurities may localize at Ca^{2+} sites, giving the weak green emission observed at around 560–580 nm.[63]

All these luminescent aluminosilicates are necessarily located on the surface of the samples, or at very small depth, otherwise the light emitted would be reabsorbed by the overlying opaque material. The attribution of these luminescent grains to albite is confirmed by their Si and Al composition measured by µ-PIXE (Fig. 5c and Table S7), with Si/Al ≈ 3.12 mass ratio perfectly matching that of alkali feldspars. This is particularly true for all the particles trapped on both sides of sample 1 (red circles), and for some of the particles in sample 2 (green circles). The particles trapped on sample 3 (blue circles) and part of those on sample 2, although showing the characteristic albite luminescence at 750–770 nm, have a lower Si/Al ratio than albite. These dust particles could therefore be an association of luminescent albite and non-luminescent, more aluminous mineral such as kaolinite $Al_2Si_2O_5(OH)_4$, giving an average ratio 3 > Si/Al > 1. Indeed, kaolinite is an alteration product of albite by the action of water in hot and humid climate, and is easily formed on the surface of albite.[64] Importantly, the fact that the same Si/Al = 3.12 ratio is measured for luminescent surface particles (Fig. 5c) and for non-luminescent aluminosilicates detected on homogeneous zones (Fig. 4c and d) is a further indication that all mineral dust is trapped on the sample surface.

As these alkali feldspar particles, associated or not with kaolinite, are trapped on both sides of the fragments, *i.e.* at the internal surface of the bitumen layers and the external surface of the linen strips, it is a clear indication that they were trapped during preparation of the mummy. Indeed, if these particles had been trapped after the mummy's excavation at the beginning of the 19th century, or even later, the dust would have been located only on the outer surfaces of the samples, which is not the case since aluminosilicate dust is more abundant on the inner surfaces. Also, the fact that these particles are also found on the internal surface of the bitumen coating of the mummy, is a first indication that this bitumen was applied to the mummy during its preparation in Ancient Egypt, and therefore it is not the result of an intervention in the first third of the 19th century.

Nature and localization of carbonate dust. Calcite $CaCO_3$ is also one of the most ubiquitous minerals in the continental crust. It is the main constituent of limestones, and is very present in Egypt, where the Nile Valley is surrounded by a vast limestone plateau.[53,65] Images of calcite microparticles are not easy to detect in µ-PIXE mappings, as Ca is a ubiquitous element in the BSM mummy. However, in addition to the red-NIR luminescence of Fe^{III} from alkali feldspar particles, µ-IBIL

spots are also abundant in the range 550 nm to 650 nm revealing the presence of carbonates particles (Fig. 6 and S7). Their Ca sites can host Mn^{II} and Fe^{II}/Fe^{III} impurities, which strongly influence the optical properties of these minerals. Contrary to feldspars, Fe^{III} is not luminescent in carbonates, and the presence of the $^4T_1 \rightarrow {}^6A_1$ emission of Mn^{II} in carbonates is highly dependent on the redox state of Fe, because Fe^{II} is a luminescence "killer".[63] So only carbonate particles whose Fe impurities are in the Fe^{III} state can show Mn^{II} luminescence. The position of the Mn^{II} emission band in carbonates is variable and depends on the strength of the crystal field, which in turn depends on both the coordination number (CN) of Mn^{II} and the length of the Mn–O bond (Fig. S6f). A variety of Mn^{II} luminescence have been reported in the literature: (i) green emission (approx. 580 nm) in aragonite (orthorhombic $CaCO_3$); (ii) yellow emission (approx. 620 nm) in calcite (trigonal $CaCO_3$); (iii) red emission (approx. 655 nm) in magnesite (trigonal $MgCO_3$); (iv) orange-red emission in dolomite ($Ca/MgCO_3$), due to the superposition of two bands around 575 nm (Mn^{II} at Ca site) and 655 nm (Mn^{II} at Mg site). Depending on the relative intensity of these two components, this results in a broad band with a single maximum intermediate between the two extreme values, or a band of composite appearance.[66]

Samples taken from the BSM mummy and from the bird mummies (corpus A) show several types of IBIL emissions attributable to carbonate particles. Fig. 6a shows two types of such particles in mappings $2\beta_1$ and $2\beta_3$ (outer strip surface), which have the higher Ca/Al ratio (Fig. 4a). The broad Mn^{II} emission band around 571 nm emitted in the bottom right of the $2\beta_1$ mapping can be due to a relatively large particle of dolomite. A different emission band around 640 nm in the $2\beta_3$ mapping is also attributable to Mn^{II} emission from three calcite particles labelled a, b and c in Fig. 6a. This luminescence band is narrower and more complex than the one in $2\beta_1$ mapping, as it shows several narrow and very weak emission lines superimposed to the Mn^{II} emission (Fig. 6b). These narrow lines are characteristic of lanthanide Ln^{3+} impurities in Ca^{2+} sites of the carbonate. Even though Ln^{3+} concentrations are very low and below the detection limit by PIXE, their very narrow optical emissions (zero–phonon transitions) make them easily detectable. Their attribution to specific lanthanide elements can be made using Dieke's diagram,[67] (Fig. 6d) and by comparing the IBIL spectrum of $2\beta_3$ mapping with that of sample 4 of corpus A, taken from a bird of prey found at Giza, where Ln^{3+} emissions are more intense (Fig. 6c and S7b). It was thus possible to identify the presence of dysprosium Dy^{3+}, samarium Sm^{3+} and neodymium Nd^{3+} in calcite of the bird of prey, and Sm^{3+}, Nd^{3+} and ytterbium Yb^{3+} ions in particles of the $2\beta_3$ mapping of the BSM mummy.

It is interesting to note that the three particles present in $2\beta_3$ mapping do not seem to have the same Ln^{3+} content, as shown by

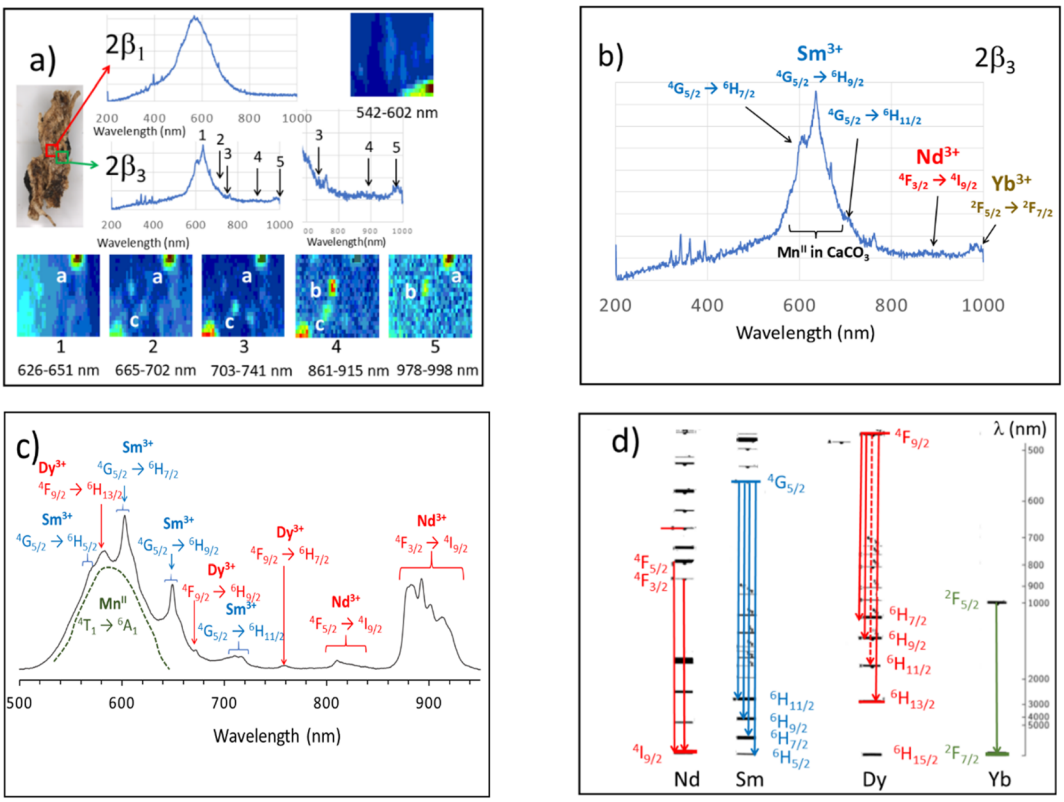

Fig. 6 Examples of μ-IBIL spectra and images of calcium carbonate microparticles trapped by mummies; (a) μ-IBIL of $2\beta_1$ and $2\beta_3$ mappings of the BSM mummy; (b) attribution of transitions due to lanthanide impurities in the Ca^{2+} site of calcite in $2\beta_3$ mapping; the narrow peaks in the 400 nm region correspond to atomic emission lines of helium; (c) zoom of the μ-IBIL spectrum of a calcium carbonate particle trapped in the black matter covering a feather of a bird of prey from Giza (sample 4 of corpus A), showing many optical transitions of Ln^{3+} impurities; this IBIL spectrum have been smoothed with a moving average (30 points); (d) partial Dieke's diagram for Nd^{3+}, Sm^{3+}, Dy^{3+} and Yb^{3+}.

the μ-IBIL images recorded in five wavelength ranges, denoted 1 to 5 in Fig. 6a. It appears that Nd^{3+} is present in the three particles, Yb^{3+} is present only in particles a and b, and Sm^{3+} dominates in particles a and c. The IBIL emissions of these three particles present an additional complexity. Indeed, Mn^{II} luminescence, which is intense at the maximum of the band (~640 nm), gives an image only for particle a, whereas particles b and c show no Mn^{II} emission. This surprising feature could be tentatively explained by the redox state of Fe impurities, recalling that Fe^{II} is a killer of Mn^{II} luminescence. The presence of Fe^{II} impurities in particles b and c could explain their absence of Mn^{II} luminescence, while Fe impurities are mostly in Fe^{III} state in particle a.

In summary, μ-IBIL spectroscopy and mapping show the variety of trace element compositions of the calcium carbonate particles trapped by the mummy, reflecting the variety of limestones formations in the geology of North east Africa.[53,65] Moreover, we observed that these carbonate particles are more abundant in the strip (in particular the outer face 2β of sample 2), while aluminosilicates are more abundant on surfaces covered with bitumen. This agrees with the hypothesis, based on Ca/Al ratio, that the mummy suffered from (at least) two dust events during its *post-mortem* history: the first one during mummification but before the application of the bitumen and the strips, with more aluminosilicates and fewer carbonates, and the other ones with more carbonates, that may have occurred after excavation of the mummy.

Mineral dust from man-made materials

In addition to airborne dust particles originating from soil erosion, the body of the deceased may have trapped particles of man-made materials present in the mummification environment. Among transition metal elements identified at trace level in the BSM mummy, Cu is present in the range 3–40 μg g^{-1} in all the mappings, with or without bitumen (Table S5). Contrary to V and Ni, which are homogeneously distributed in the bitumen, Cu is present in μ-PIXE mappings only in the form of small spots, either in bitumen or in linen strips, indicating the presence of Cu-rich particles. They were observed also in several mummies in corpus A (birds) and corpus B (rams, crocodile and human). Two examples are shown in Fig. S8. Contrary to V and Ni elements, Cu is nearly absent from pure Dead Sea bitumen (<3 μg g^{-1} in DS sample, Table S5 and Fig. S8), which was the source of bitumen for the mummies in corpus A and B.[16] This ubiquitous presence of Cu-rich spots in these mummies indicates that they are due to trapped mineral dust particles that were present in ambient atmosphere of the mummification site. It is difficult to determine the nature of these particles in the absence of other characteristic chemical elements. However, a number of them show a near infrared (NIR) IBIL emission centered at 900–910 nm. A good example of such NIR μ-IBIL mapping associated to Cu is shown for particles trapped on the surface 2β of a linen strip fragment (Fig. 7). It shows the presence of at least three NIR spots with emission peaking around 900 nm (Fig. 7b), corresponding to Cu spots in μ-PIXE mapping (Fig. 7c). This optical luminescence is intense compared to the X-ray emissions, to such an extent that when the NIR emission is weaker, the X-ray emission becomes barely detectable. This is the case for the particle near the center of the mapping in Fig. 7, where the X-ray emission of Cu, marked by the white arrow, is barely visible compared to its NIR emission.

This strong NIR emission is typical of "Egyptian Blue" (EB), an artificial pigment used in Egypt since the 4th millennium BC and composed mainly of cuprorivaite $CaCuSi_4O_{10}$.[68] While there are many materials in which copper is luminescent in the Cu^{I}

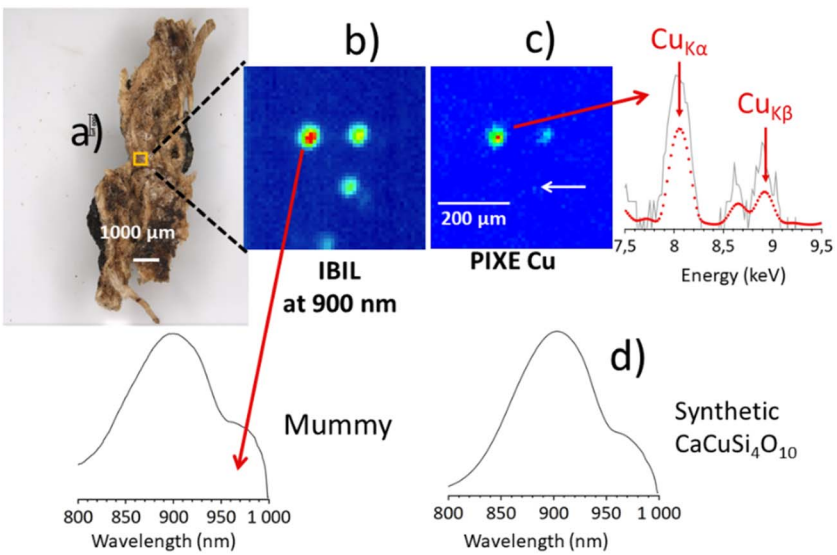

Fig. 7 μ-IBIL and μ-PIXE mappings performed on a 500 × 500 μm^2 area of the external surface 2β of a strip fragment from the BSM mummy; (a) photograph of the outer surface of the sample, the mapped area is represented by a yellow square; (b) μ-IBIL mapping around 900 nm showing 4 luminescent spots, 3 of which being intense, with the μ-IBIL spectrum of the most intense spot; (c) μ-PIXE mapping of the K_α and K_β transitions of Cu, and portion of the μ-PIXE spectrum (theoretical spectrum in red) corresponding to the most intense spot. The white arrow indicates the position of a spot of very low intensity, but visible to the naked eye; (d) IBIL spectrum of a sample of cuprorivaite $CaCuSi_4O_{10}$ synthesized in the laboratory; IBIL spectra have been smoothed with a moving average (30 points).

state ($3d^8$ configuration), there are very few in which it is the Cu^{II} ion ($3d^7$ configuration) that is luminescent.[69] Among the exceptions are certain minerals of the gillespite group ($BaFeSi_4O_{10}$) with the composition $MCuSi_4O_{10}$, with $M = Ca^{2+}$ (cuprorivaite, the main component of EB), $M = Ba^{2+}$ (effenbergite, the "Chinese blue"), and $M = Sr^{2+}$ (wesselsite). These minerals are rare in nature, but EB is a synthetic pigment that was ubiquitous in ancient Egypt. The structure of cuprorivaite and the origin of its NIR emission are described in Fig. S6a and b. Proof that these luminescent particles are indeed due to EB is provided by the fact that exactly the same IBIL spectrum was obtained with a cuprorivaite sample synthesized in our laboratory (Fig. 7d).[70]

The EB particles shown in Fig. 7 were trapped in linen fibers of the strip. However, EB was also observed in the bitumen covering the mummy, albeit less clearly (Fig. S9a and b), showing that these particles were deposited during the preparation of the mummy. The situation is not always as simple as in Fig. 7, because on the one hand, the NIR band of the particles in Fig. S9a and b is broad and rather centered around 920–960 nm, indicating that they are probably the superposition of several emission bands in the same wavelength range. On the other hand, many of these Cu-rich particles do not exhibit NIR luminescence, even when they are close to other luminescent EB particles (compare Fig. 7, S9c and d). This absence of NIR luminescence in some Cu-rich particles can be explained by the fact that they are buried beneath the surface of the material, close enough to the surface for Cu–K photons to escape, but deep enough for the NIR emission to be absorbed by the overlying matter. Another possible reason for the absence of luminescence in certain Cu-rich particles could be that they originate from contamination from the bronze tools used to prepare the mummy (see Section S4.3 for more details).

The fact that EB dust, a material synthesized by the ancient Egyptians, is also found with other airborne mineral particles in some bird mummies (Fig. S4), whose ages and burial sites are known, is another argument in favor of the antiquity of the application of the pure bitumen layer on the BSM mummy. The presence of trapped EB particles would not be expected in the early 19th century. Indeed, EB was widely used throughout Egyptian antiquity and remained the only blue pigment during Roman antiquity.[68] Its production then declined and ceased rather abruptly at the end of the Western Roman Empire and during the Early Middle Ages (5th–7th centuries). EB was used only very occasionally from the 8th to the 16th century, without it being known whether it was manufactured, imported or recovered from ancient Roman objects or ruins. Knowledge of EB then disappeared completely for almost 300 years, until chemists took a new interest in the 19th century and figured out how to synthesize it. However, even in the last quarter of the 19th century, the exact structure and composition of EB was still unknown, and chemists did not know how to reproduce it.[71] The synthesis of EB was really mastered in the beginning of the 20th century,[72] and it was not until the 1950s that a definitive link was established between EB and the rare but naturally occurring mineral cuprorivaite $CaCuSi_4O_{10}$.[73]

Consequently, the presence of EB in bitumen and strips of the BSM mummy indicates that it has not been polluted by EB dust in the early 19th century, as this material was virtually forgotten at the time. Instead, it appears far more likely that these EB particles were deposited on the mummy during its preparation in a place and time where EB was ubiquitous. This confirms once again that the layer of bitumen has not been applied in the early 19th century to restore the mummy to make it more attractive, as was initially suspected.[8] All these results on trapped dust provide strong arguments in favor of the antiquity of the application of the pure bitumen of unknown origin on the BSM mummy.

The case of Hg and Pb impurities

Mercury (Hg), lead (Pb) and arsenic (As) are often associated with the most persistent forms of pesticides used to preserve museum collections,[74,75] and these elements are also present in modern anthropogenic pollution (gasoline-powered vehicles before 1990, industry, agriculture, …). Arsenic is virtually absent from all μ-PIXE mappings of the BSM mummy, as well as the mummies in corpus A and B (Table S8). In contrast, we observed the omnipresence of Hg in μ-PIXE spectra, with variable concentrations in the range 34 to 2100 μg g^{-1} (Table S8). This contamination is clearly visible in the μ-PIXE spectra in Fig. 3, where Hg is identifiable by its X-ray lines (L_α: 10 keV, L_β: 11.8 keV and L_γ: 13.8 keV), which are particularly visible on the inner face 2α covered with a thick layer of bitumen (Fig. 3a). Hg is also present in the outer face 2β, made up of clean linen fibers with very little bitumen in some places, in association with Pb (L_α: 10.5 keV, L_β: 12.6 keV and L_γ: 14.8 keV) (Fig. 3b). Their quantification reveals that Hg and Pb do not have the same origin and localization, as shown in Fig. 8a, which represents Hg against Pb concentrations in all the surfaces scanned by the proton beam. Hg contamination is larger (600 to 2100 μg g^{-1}), and Pb concentration is lower (10 to 40 μg g^{-1}) on surfaces covered with a thick layer of bitumen (2α and 3α). In contrast, Hg concentration is lower (<160 μg g^{-1}) and Pb concentration higher (60 to 180 μg g^{-1}) when the surfaces being probed are made up of clean linen fibers (2β) or linen strips more or less impregnated with a thin layer of black matter (1α and 1β). These results suggest that Pb impurities are mainly located in the strips, while Hg impurities are located both in the black matter and in the strips.

Pure bitumen does not show any Hg and Pb contamination (yellow square in Fig. 8a). Hg is also absent in all the other mummies analyzed in this work (corpus A and B), while Pb is found at trace levels in all these mummies (Table S8). The presence of mercury is therefore specific to the BSM mummy alone. A clue to the origin of this Hg contamination is provided by the $2\alpha'_4$ and $2\beta_2$ μ-PIXE mappings (Fig. 8b and 9). $2\alpha'_4$ mapping is the same as $2\alpha_4$, but with a larger surface area (1000 × 1000 μm^2). It shows a local over-concentration of Hg with no clear contour at the top left of the scanned surface, with a corresponding diffuse over-concentration of Cl (K_α: 2.62 keV and K_β: 2.81 keV). The contrast is less clear-cut for Cl than for Hg, as Cl is omnipresent in the mummy samples, as well as in the

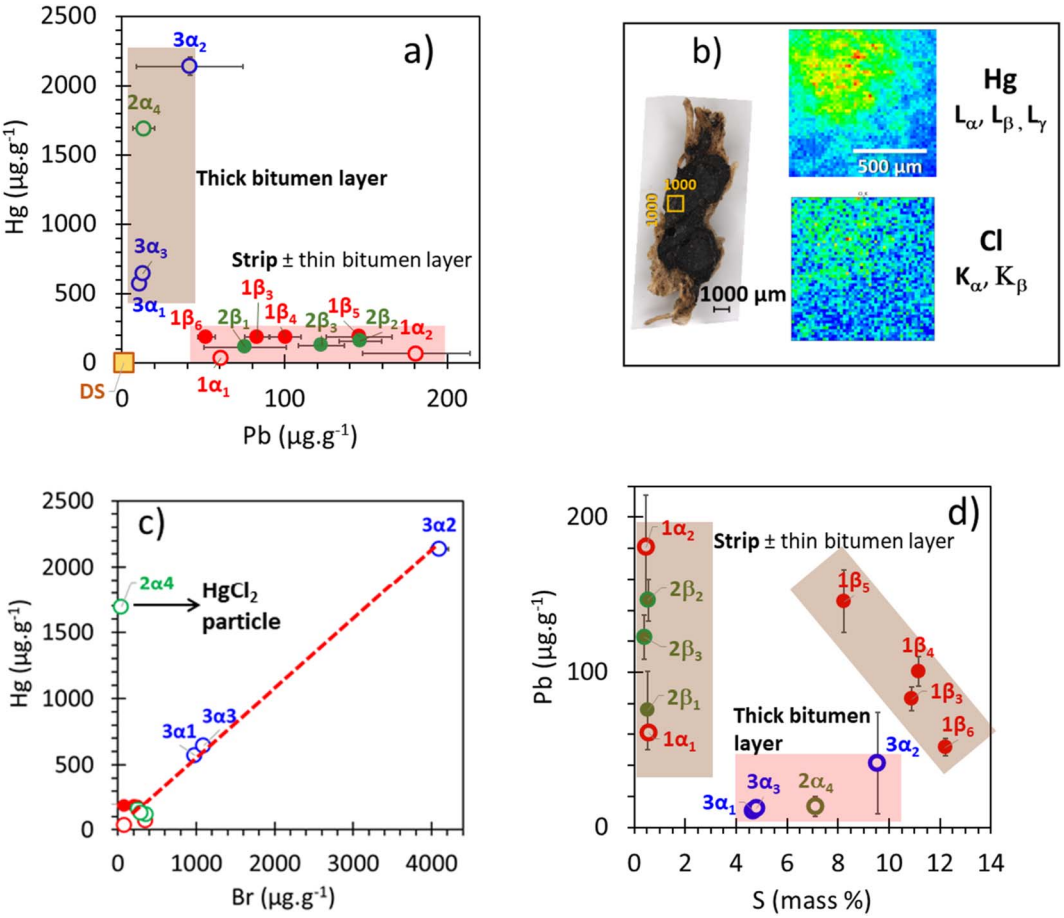

Fig. 8 Hg, Pb and Br contents measured on homogeneous zone of samples of the BSM mummy; (a) Hg *versus* Pb; (b) µ-PIXE images of Hg and Cl in $2\alpha'_4$ mapping; (c) Hg *versus* Br; (d) Pb *versus* S.

reference bitumen (Table S8). The size of this Hg-rich spot is approximately 500 × 500 µm^2. This result strongly suggest the presence of $HgCl_2$, a highly toxic compound that has been used in museums in the 19th and early 20th centuries to protect objects made of organic materials such as wood, paper and textiles against fungi and insect infestation.[74,76]

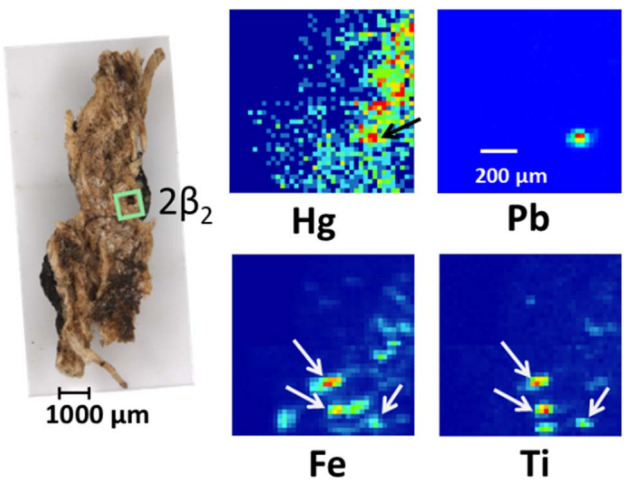

Fig. 9 µ-PIXE image of Hg, Pb, Fe and Ti in $2\beta_2$ mapping. The black arrow indicates the presence of Hg on the PbS particle. White arrows indicate the presence of grains with both Fe and Ti.

The highest Hg contents are found on the inner faces 2α (which contain the $HgCl_2$ grain) and 3α (Fig. 8a). Surprisingly, the three 3α mappings show a linear correlation between Hg and Br rather than Cl (Fig. 8c and Table S8), which might suggest that the mummy was also treated with $HgBr_2$, another highly toxic mercury salt. However, $HgBr_2$ has been much less used than $HgCl_2$ for disinfecting and protecting organic objects in natural history collections.[74] It is important to note that the $HgCl_2$ grain shown in the $2\alpha'_4$ mapping does not contain Br (Fig. 8b and c). We must therefore admit that the BSM mummy underwent at least two different protective treatments, one with $HgCl_2$ and the other with $HgBr_2$. These mercury salts are very stable and have low volatility, so that they persist on treated objects for decades or even over a century or more.[74,77,78]

The fact that the highest Hg contents are found on inner surfaces covered by a thick layer of bitumen indicates that these biocide compounds have been more strongly and persistently fixed in the bitumen coating than in linen fibers. It also shows that the inner surfaces of the samples (facing the mummy) were accessible when the Hg treatment was performed, implying that the strips were already partially removed, like the actual

mummy exposed in the museum. The Hg treatment therefore took place after the mummy had been acquired and displayed. There is no indication of treatment of the mummy with mercury salts in the archives of the *Musée de Boulogne-sur-Mer*. As the BSM mummy spent some time at the *Musée de l'Homme* in Paris, in 1932–1934,[79] it seems possible that undocumented treatments with mercury were carried out during its stay at this museum. Also, it cannot be ruled out that these treatments were carried out before 1837, when the mummy was in the possession of a private Parisian collector. While $HgCl_2$ is mentioned in the literature for the treatment of mummies,[54] no work to our knowledge mentions the use of $HgBr_2$ for such a purpose. If this result is confirmed, the BSM mummy would be an exception.

Pb is present at trace level in all the studied mummies (Table S8), suggesting that this element is present as impurities in mineral dust trapped by mummies. In the BSM mummy, Pb is present in much lower concentrations than Hg, and do not exceed 180 μg g^{-1}. An indication of the location of Pb impurities can be deduced from the diagram representing the Pb content *versus* the S content, the latter giving information on the quantity of bitumen probed by the proton beam (Fig. 8d). This diagram indicates that Pb concentrations are very low on surfaces covered with a thick layer of bitumen (2α and 3α) and higher on surfaces with only clean linen fibers (2β) or a very thin layer of organic matter covering linen, allowing protons to pass through (1α). This is confirmed by the external face 1β, which

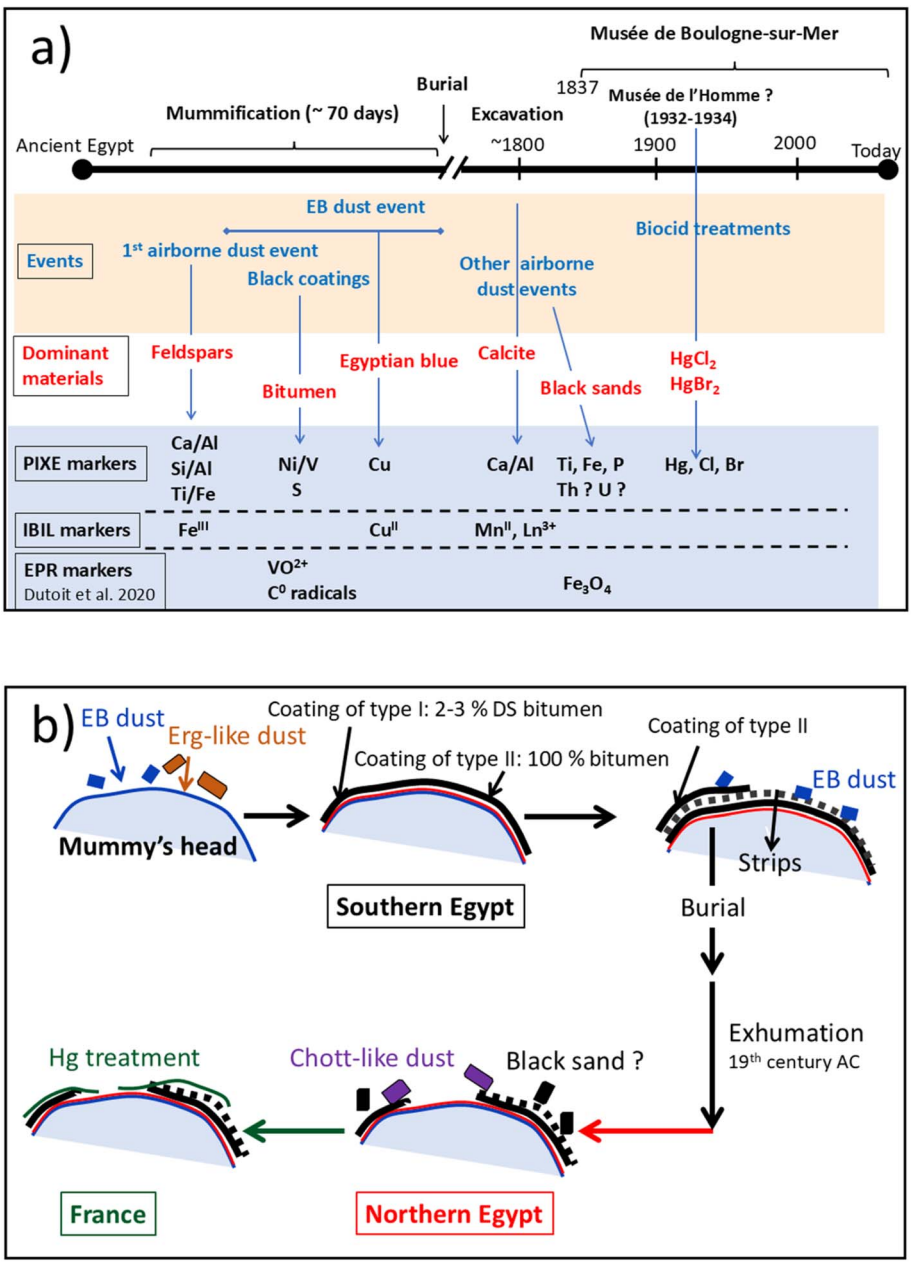

Fig. 10 An attempt to reconstruct the post-mortem history of the BSM mummy using trace elements; (a) the different PIXE, IBIL and EPR markers; (b) schematic representation of the succession of events.

has varying thicknesses of bitumen, with thick drips in places (Fig. 1b). It is clear that the Pb content decreases as the thickness of the bitumen (*i.e.* the amount of S) through which the proton beam is passing increases.

The difference of situation of Hg and Pb impurities is well illustrated in the case of $2\beta_2$ μ-PIXE mapping (Fig. 9), showing that Pb is concentrated in one single particle while Hg is more homogeneously distributed on the surface, reflecting the mummy's treatment with $HgCl_2$. To establish the nature of the Pb-rich grain, a 16-pixel square ROI of this grain was analyzed. Pb was quantified from its M line (2.35 keV), closer in energy to the K_β line of S (2.46 keV) rather than its L_β line (12.6 keV), in order to probe the same sample volume. It was therefore possible to obtain a rough estimate of the mass ratio Pb/S ≈ 8.78, which corresponds to an atomic ratio Pb/S ≈ 1.35. Although subject to important uncertainty, this ratio is compatible with the presence of a PbS particle trapped by linen fibers. PbS was a material central to the daily lives of the Egyptians, for example for women's and men's make-up (kohl), but also to make-up mummies or their funerary masks. The grain in Fig. 9 may come from an accidental fall of a PbS particle from the make-up of a priest preparing the mummy, or from the mummy's inner coffin. An argument in favor of the anteriority of the PbS grain to the $HgCl_2$ treatment is the presence of an excess of Hg superimposed to this PbS grain (black arrow in Fig. 9), whereas one would expect a deficiency of Hg if the $HgCl_2$ treatment had preceded the capture of this grain.

Other minerals

The $2\beta_2$ μ-PIXE mapping in Fig. 9 gives also an idea of the speciation of Fe and Ti elements in dust trapped in strips of the BSM mummy. The Ti/Fe = 0.1 average ratio of this mapping corresponds exactly to that of the continental crust (Fig. 4b). Three different types of particles can be distinguished: those containing only Ti which correspond to TiO_2 particles, those containing only Fe which correspond to Fe oxides, and those containing both Fe and Ti in similar quantities (marked with white arrows). The latter may correspond to ilmenite $FeTiO_3$, a magmatic rock mineral found in abundance in the black sands along the coast of the Nile delta. These black sands contain ilmenite ($FeTiO_3$), magnetite (Fe_3O_4), garnet ($X^{2+}{}_3Y^{3+}{}_2(SiO_4)_3$), zircon ($ZrSiO_4$), rutile ($TiO_2$) and monazite ($Ln,Th(PO_4)$) in decreasing order of abundance.[80] The presence of ferromagnetic Fe_3O_4 microparticles in samples of the BSM mummy was already demonstrated by EPR spectroscopy.[8] Although we did not detect zircon in $2\beta_2$ mapping (Zr content is below the LOD of 12 μg g^{-1}), the presence of garnet is possible given that this mapping contains 4500 μg g^{-1} of Si. The presence of monazite is also possible given that $2\beta_2$ mapping contains 965 μg g^{-1} of P. Quantification of Th (M_α line: 3.0 keV) and U (M_α line: 3.17 keV), two elements present as impurities in monazite and zircon, gives 546 ± 12 μg g^{-1} (LOD = 60 μg g^{-1}) for Th, and 295 ± 21 μg g^{-1} (LOD = 124 μg g^{-1}) for U. Although these concentrations must be considered with extreme caution, it should be noted that the black sands of the Nile Delta are known to be radioactive, because of their high Uranium and Thorium content.[81]

This $FeTiO_3$, Fe_3O_4, TiO_2 (and possibly monazite) mineral association characteristic of black sands, along with the presence of chott-like dust with high Ca/Al ratio (Fig. 4a) on the surface of strips, are indications that the mummy most probably stayed in northern Egypt before leaving for Europe at the beginning of the 19th century. Interestingly, these black sands constitute major deposits along the coasts of Damietta and Rosetta,[80] which saw the passage of Napoleon Bonaparte's army and the scientists who accompanied him on the Egyptian expedition of 1798–1799. If the BSM mummy and its coffins were brought back on this expedition (which has not been proven), as written on the coffin, then this mummy may well have felt the sea wind carrying this black dust.

Conclusion

The combination of ion-beam techniques (μ-PIXE-EBS and μ-PIXE-IBIL) is a promising methodology for studying the provenance and manufacturing of inorganic materials in cultural heritage.[82–84] To our knowledge, the combination of PIXE-EBS-IBIL has never been used before for the analysis, in a forensic approach, of complex bioorganic systems such as mummies. In this work, fragments detached from the neck and head of the Egyptian mummy of an unknown man, conserved at the *Musée de Boulogne-sur-Mer* (BSM), and samples from 14 other Egyptian mummies (birds, rams, crocodile, human) have been analyzed non-destructively at the nuclear microprobe AGLAE facility. The original character of the BSM mummy is that it was partially covered with a pure bitumen layer showing no trace of chemical degradation, as recently shown by EPR and GC-MS analyses.[8] As this mummy was acquired by the museum in 1837 from a private collector, it has been suspected that this pure bitumen coating came from an early restoration to improve the sale of the coffin/mummy ensemble, a common practice in the 19th century. In order to trace the *post-mortem* history of the mummy, we used μ-PIXE and μ-IBIL of trace elements present in the bitumen and airborne micro-dust captured by the strips and the bitumen. This combined analysis has led to several conclusions and hypotheses on the mummy's post-mortem history, summarized on Fig. 10:

(i) Quantification of the trace elements V and Ni in the bitumen layer covering the BSM mummy showed that its source was not the Dead Sea, – the most frequent source of bitumen in ancient Egypt, and also the source of bitumen of the other mummies analyzed in this work. In addition to this pure bitumen coating of unknown origin, traces of black matter containing 2–3% of Dead Sea bitumen were also detected below the strips.

(ii) Microparticles of Egyptian blue (EB) pigment, identified by the presence of Cu-rich spots and their NIR luminescence, were detected on both sides of the samples. They may have been component of the airborne dust in the mumification site. The presence of this pigment, a material synthesized by the ancient Egyptians, and forgotten from the Middle Ages onwards and still poorly understood in the first half of the 19th century, is an indication that the pure bitumen layer was applied during the preparation of the mummy in the antiquity, and not in the 19th century.

(iii) The presence of abundant alkali feldspar microparticles on both sides of the samples, recognizable by their Si/Al ratio and the luminescence of Fe^{III} impurities, is a second indication that they were trapped in the antiquity, before application of the black coating. Indeed, these minerals are abundant in desert sand, and therefore a major component of the airborne dust in the mummification environment. The fact that abundant Saharan dust could have settled on the BSM mummy during preparation indicates that the embalming workshop was probably well ventilated, to avoid the nuisance of a putrefying body.

(iv) Abundant calcite particles are also present in the samples, and were identified by the luminescence of Mn^{II} impurities and of some traces Ln^{3+} elements (Sm, Dys, Nd and Yb), all these elements being localized at the Ca^{2+} site of the carbonate mineral. The Ca/Al ratio shows that calcite dust particles (luminescent or not) are predominantly localized at the external surface of the strips.

(v) The predominance of aluminosilicate particles over carbonates on the inner surfaces of the samples, while the opposite is true on the outer surfaces, suggests that the mummy was subjected to (at least) two different airborne dust inputs (Fig. 10): a first input of sand from Sahara (Ca/Al < 2), probably in spring, during the preparation of the mummy in southern Egypt, but before the bitumen coating and the strips were applied, and a second input of carbonate-rich dust from Northern Egypt (2< Ca/Al < 10). It is likely that this second dust event took place after the mummy had been excavated from its site (in the Thebes region) and removed from the coffins. This event could have taken place in northern Egypt in the early 19th century, before the mummy and coffins were shipped to France. The presence, on the outer surface of the strips, of a mineral association ilmenite + rutile + magnetite (+monazite?) characteristic of the black sands of the Nile delta, is an argument in favor of this hypothesis.

(vi) PIXE analysis also showed significant Hg contamination attributed to $HgCl_2$ and possibly $HgBr_2$. It was concluded that the mummy must have undergone undocumented disinfection campaigns by mercury salts, highly toxic compounds used until the 20th century to protect museum collections against insects and fungi.

Although several hypotheses concerning the post-mortem history of the BSM mummy remain to be confirmed, this work shows the potential of combined μ-PIXE and μ-IBIL spectroscopy and mapping to trace the evolution of the mummy's environment over time.

Author contributions

DG: Conceptualization, methodology, interpretation of IBIL and PIXE, writing original draft, review and editing; OA: nuclear microprobe experiments and data curation; QLM: nuclear microprobe experiments, help in data curation; LP: improving IBIL setup; TC: EBS analyses, interpretation of PIXE; ALD: Project administration; LB: supervision, interpretation of IBIL, validation.

Conflicts of interest

There are no conflicts of interest to declare.

Data availability

Supplementary information (SI): PIXE, EBS and IBIL spectra, and the data (Tables S2–S8). See DOI: **https://doi.org/10.1039/d5ja00339c**.

Acknowledgements

We would like to thank Gaelle Etesse, Head of the collection department, *musée de Boulogne-sur-Mer*, for her invaluable information on the mummy of the unknown man. Didier Berthet, curator at the *Musée des Confluences*, Lyon, is gratefully acknowledged for providing us with samples from the museum's bird mummies.

References

1 P. Tresson, *Catalogue descriptif des Antiquités égyptiennes de la salle Saint-Ferriol, Grenoble, Cat.n°*, 1933, vol. 48, pp. 72–75.
2 M. Dewachtez, Imbroglio Djedmoutefänkh et Psamétique, Le Cabinet d'Uriage et sa contribution aux débuts de l'égyptologie (1841-1916), in *Le château d'Uriage, son cabinet de curiosité*, Chapö Public Editions, 2008, pp. 48–62.
3 J. Yoyotte, La momie de Boulogne-sur-Mer, in *Les cahiers du vieux Boulogne*, 1981, vol. 11, pp. 3–9.
4 H. Wallon, *Notice sur la vie et les travaux de François-Auguste-Ferdinand Mariette-Pacha, membre ordinaire de l'Académie des Inscriptions et Belles Lettres*, 1883, Firmin-Didot. **http://archive.org/details/noticesurlaviee00wallgoog**.
5 F. Halley-des-Fontaines-Poiret, C. Ziegler, and C. Devauchelle, *Des dieux, des tombeaux, un savant: En Égypte, sur les pas de Mariette pacha*, Somogy Editions d'Art, 2004 1ère édition, Paris.
6 P. Dal-Prà, *Rapport de restauration de la momie d'homme du Château-Musée de Boulogne sur Mer. N°6306*, C2RMF, 2004, Paris.
7 F. Vincent, *Intervention concernant la momie d'homme, Château-Musée de Boulogne-sur-Mer, N°6307*, C2RMF, 2004, Paris.
8 C. E. Dutoit, L. Binet, H. Fujii, A. Lattuati-Derieux and D. Gourier, *Anal. Chem.*, 2020, **92**, 15445–15453, DOI: **10.1021/acs.analchem.0c03116**.
9 S. A. Buckley and R. P. Evershed, *Nature*, 2001, **413**, 837–841, DOI: **10.1038/35101588**.
10 M. Ménager, C. Azémard and C. Vieillescazes, *Microchem. J.*, 2014, **114**, 32–41, DOI: **10.1016/j.microc.2013.11.018**.
11 J. Lucejko, J. Connan, S. Orsini, E. Ribechini and F. Modugno, *J. Archaeol. Sci.*, 2017, **85**, 1–12, DOI: **10.1016/j.jas.2017.06.015**.
12 R. Brettell, W. Martin, S. Atherton-Woolham, B. Stern and L. McKnight, *Stud. Conserv.*, 2017, **62**, 68–82, DOI: **10.1179/2047058415Y.0000000027**.

13 J. Jones, F. G. Higham, D. Chivall, R. Bianucci, G. L. Kay, M. J. Pallen, R. Oldfield, F. Ugliano and S. A. Buckley, *J. Archaeol. Sci.*, 2018, **100**, 191–200, DOI: 10.1016/j.jas.2018.07.011.

14 K. Fulcher, M. Serpico, J. H. Taylor and R. Stacey, *Proc. Natl. Acad. Sci. U. S. A.*, 2021, **118**, e2100885118, DOI: 10.1073/pnas.2100885118.

15 J. Hertzog, H. Fujii, R. Zostautaite, A. Lattuati-Derieux, P. Richardin, V. Carré, A. Aubriet and P. Schmitt-Kopplin, *J. Archaeol. Sci.: Rep.*, 2022, **48**, 103861–103870, DOI: 10.1016/j.jasrep.2023.103861.

16 O. Anduze, D. Gourier, L. Binet, A. Malergue, V. Grossi and A. Lattuati-Derieux, *J. Anal. At. Spectrom.*, 2025, **40**, 487–497, DOI: 10.1039/D4JA00442F.

17 J. Connan and D. Dessort, *C. R. Acad. Sci., Ser. II*, 1991, **312**, 1445–1452, DOI: 10.1098/rstb.1999.0358.

18 K. A. Clark, S. Ikram and R. P. Evershed, *Philos. Trans. R. Soc., A*, 2016, **374**, 20160229, DOI: 10.1098/rsta.2016.0229.

19 P. I. Premović, I. R. Tonsa, M. S. Pavlović, L. López and S. LoMonaco, *Fuel*, 1998, **77**, 1769–1776, DOI: 10.1016/S0016-2361(98)00100-8.

20 C. E. Dutoit, L. Binet, H. Vezin, O. Anduze, A. Lattuati-Derieux and D. Gourier, *Magn. Reson.*, 2022, **3**, 111–124, DOI: 10.5194/mr-3-111-2022.

21 J. Maurer, T. Möhring and J. Rullkötter, *J. Archaeol. Sci.*, 2002, **29**, 751–762, DOI: 10.1006/jasc.2001.0773.

22 J. A. Harrell and M. D. Lewan, *Archaeometry*, 2002, **44**, 285–295, DOI: 10.1111/1475-4754.t01-1-00060.

23 J. Connan and T. Van de Velde, *Arab. Arch. Epig.*, 2010, **21**, 1–19, DOI: 10.1111/j.1600-0471.2009.00321.x.

24 A. Nissenbaum and S. Buckley, *Archaeometry*, 2013, **55**, 563–568, DOI: 10.1111/j.1475-4754.2012.00713.x.

25 K. Fulcher, R. Stacey and N. Spencer, *Sci. Rep.*, 2020, **10**, 8309, DOI: 10.1038/s41598-020-64209-8.

26 A. J. G. Barwise, *Energy Fuels*, 1990, **4**, 647–652, DOI: 10.1021/ef00024a005.

27 G. N. Breit and R. B. Wanty, *Chem. Geol.*, 1991, **91**, 83–97, DOI: 10.1016/0009-2541(91)90083-4.

28 F. Galarraga, K. Reategui, A. Martinez, J. F. Llamas and G. Marquez, *J. Sci. Eng.*, 2008, **61**, 9–14, DOI: 10.1016/j.petrol.2007.10.001.

29 L. López and S. Lo Mónaco, *Org. Geochem.*, 2017, **104**, 53–68, DOI: 10.1016/j.orggeochem.2016.11.007.

30 N. R. Foster, B. Martin, J. Hoogerwerff, M. G. Aberle, B. de Caritat, P. Roffey, R. Edwards, A. Malik, P. Thwaites, M. Waycott and J. Young, *Forensic Sci. Int.*, 2023, **344**, 111599, DOI: 10.1016/j.forsciint.2023.111599.

31 D. Pirrie, L. Dawson and G. Graham, *Episods*, 2017, **40**, 141–147, DOI: 10.18814/epilugs/2017/v40i2/017016.

32 F. Lucarelli, *Eur. Phys. J. Plus*, 2020, **135**, 538, DOI: 10.1140/epjp/s13360-020-00516-3.

33 L. Pichon, B. Moignard, Q. Lemasson, C. Pacheco and Ph. Walter, *Nucl. Instrum. Methods Phys. Res., Sect. B*, 2014, **318**, 27–31, DOI: 10.1016/j.nimb.2013.06.065.

34 L. Pichon, T. Calligaro, Q. Lemasson, B. Moignard and C. Pacheco, *Nucl. Instrum. Methods Phys. Res., Sect. B*, 2015, **348**, 68–72, DOI: 10.1016/j.nimb.2015.01.010.

35 J. F. Ziegler, M. D. Ziegler and J. P. Biersack, *Nucl. Instrum. Methods Phys. Res., Sect. B*, 2010, **268**, 1818–1823, DOI: 10.1016/j.nimb.2010.02.091.

36 S. A. E. Johansson, and J. L. Campbell, *PIXE: A Novel Technique for Elemental Analysis*. John Wiley & Sons, New York. DOI: 10.1002/xrs.1300180514.

37 L. Pichon, T. Calligaro, V. Gonzalez, Q. Lemasson, B. Moignard and C. Pacheco, *Nucl. Instrum. Methods Phys. Res., Sect. B*, 2015, **363**, 48–54, DOI: 10.1016/j.nimb.2015.01.086.

38 J. L. Campbell, N. I. Boyd, N. Grassi, P. Bonnick and J. A. Maxwell, *Nucl. Instrum. Methods Phys. Res., Sect. B*, 2010, **268**, 3356–3363, DOI: 10.1016/j.nimb.2010.07.012.

39 V. A. Solé, E. Papillon, M. Cotte, P. Walter and J. Susini, *Spectrochim. Acta, Part B*, 2007, **62**, 63–68, DOI: 10.1016/j.sab.2006.12.002.

40 W. Eckstein and M. Mayer, *Nucl. Instrum. Methods Phys. Res., Sect. B*, 1999, **153**, 337–344, DOI: 10.1016/S0168-583X(98)01011-8.

41 E. B. Yatsishina, V. M. Pozhidaev, Ya. E. Sergeeva, V. M. Retivov, E. Yu. Tereshchenko, I. S. Kulikova and E. I. Panarina, *J. Anal. Chem.*, 2021, **76**, 779–784, DOI: 10.1134/S1061934821040122.

42 W. Sh. El Diasty and K. E. Peters, *J. Pet. Geol.*, 2014, **37**, 105–126, DOI: 10.1111/jpg.12573.

43 R. F. Marschner and H. T. Wright, *Archaeological Chemistry-II*, 1978, **171**, 150–171, DOI: 10.1021/ba-1978-0171.ch010.

44 J. Connan, *Phil. Trans. R. Soc. Lond. B*, 1999, **354**, 33–50.

45 B. P. Tissot, and D. H. Welte, *Petroleum Formation and Occurrence*, Springer Verlag, 2nd edition, 1984, Berlin, Heidelberg.

46 D. Scheuvens, L. Schütz, K. Kandler, M. Ebert and S. Weinbruch, *Earth-Sci. Rev.*, 2013, **116**, 170–194, DOI: 10.1016/j.earscirev.2012.08.005.

47 M. Boraly, M. El-Metwally, A. Borbon, S. Chevaillier, B. Laurent, S. Lafon, F. F. El Sanabary, M. Masmoudi and S. C. Alfaro, *Int J Environ. Sci. Technol.*, 2024, **21**, 1875–1888, DOI: 10.1007/s13762-023-05077-3.

48 S. Nowak, S. Lafon, S. Caquineau, E. Journet and B. Laurent, *Talanta*, 2018, **186**, 133–139, DOI: 10.1016/j.talanta.2018.03.059.

49 S. R. Taylor, *Geochim. Cosmochim. Acta*, 1964, **28**, 1273–1285, DOI: 10.1016/0016-7037(64)90129-2.

50 S. Schiødt, *Medical Sciences in Ancient Egypt: a Translation and Interpretation of Papyrus Louvre-Carlsberg*, PhD thesis, University of Copenhagen, 2021.

51 K. Schepanski, *Geosciences*, 2018, **8**, 151, DOI: 10.3390/geosciences8050151.

52 J. Nicolás, M. Chiari, J. Crespo, I. Garcia Orellana, F. Lucarelli, S. Nava, C. Pastor and E. Yubero, *Atmos. Environ.*, 2008, **42**, 8872–8882, DOI: 10.1016/j.atmosenv.2008.09.018.

53 Z. Hammimi, A. El-Barkooky, J. M. Frias, H. Fritz, and Y. Abd El-Rahman, *The Geology of Egypt* Springer, 2020, London.

54 A. C. Aufderheide, *The Scientific Study of Mummies* Cambridge University Press. 2003.

55 D. J. Telfer and G. Walker, *Nature*, 1975, **258**, 694–695, DOI: **10.1038/258694a0**.

56 J. E. Geake, G. Walker, D. J. Telfer and A. A. Mills, *Philos. Trans. R. Soc. London. Ser. A*, 1977, **285**, 403–408.

57 R. J. Brooks, A. A. Finch, D. E. Hole, P. D. Townsend and Z. L. Wu, *Contrib. Mineral. Petrol.*, 2002, **143**, 484–494, DOI: **10.1007/s00410-002-0359-4**.

58 R. Visocekas, C. Barthou and Ph. Blanc, *Radiat. Meas.*, 2014, **61**, 52–73, DOI: **10.1016/j.radmeas.2013.11.002**.

59 A. A. Finch and J. Klein, *Contrib. Mineral. Petrol.*, 1999, **135**(2), 234–243, DOI: **10.1007/s004100050509**.

60 N. R. J. Poolton, L. Bøtter-Jensen and O. Johnsen, *Radiat. Meas.*, 1996, **26**(1), 93–101, DOI: **10.1016/1350-4487(95)00288-X**.

61 M. R. Krbetschek, J. Götze, A. Dietrich and T. Trautmann, *Radiat. Meas.*, 1997, **27**(5), 695–748, DOI: **10.1016/S1350-4487(97)00223-0**.

62 M. R. Krbetschek, J. Götze, G. Irmer, U. Rieser and T. Trautmann, *Min. Petr.*, 2002, **76**, 167–177, DOI: **10.1007/s007100200039**.

63 J. Götze, *Anal. Bioanal. Chem.*, 2002, **374**, 703–708, DOI: **10.1007/s00216-002-1461-1**.

64 C. Tchoubar, *Bull. Soc. Fr. Mineral. Cristallogr.*, 1965, **LXXXVIII**, 483–518.

65 A. Borghi, D. Angelici, M. Borla, D. Castelli, A. d'Atri, G. Gariani, A. Lo Giudice, L. Martire, A. Re and G. Vaggelli, *Rend. Lincei.*, 2015, **26**, 385–398, DOI: **10.1007/s12210-015-0441-2**.

66 D. K. Richter, T. H. Götte, J. Götze and R. D. Neuser, *Mineral. Petrol.*, 2003, **79**, 127–166, DOI: **10.1007/s00710-003-0237-4**.

67 R. T. Wegh, A. Meijerink, R. J. Lamminmäki and J. Hölsä, *J. Lumin.*, 2000, **87–89**, 1002–1004, DOI: **10.1016/S0022-2313(99)00506-2**.

68 M. Nicola, R. Gobetto and A. Masic, *Rend. Lincei. Sci. Fis. Nat.*, 2023, **34**(2), 369–413, DOI: **10.1007/s12210-023-01153-5**.

69 G. Blasse, and B. C. Grabmaier, *Luminescent Materials*, Springer Verlag, 1994, New York, Berlin.

70 L. Binet, J. Lizion, S. Bertaina and D. Gourier, *J. Phys. Chem. C*, 2021, **125**(45), 25189–25196, DOI: **10.1021/acs.jpcc.1c06060**.

71 M. F. Fouqué, *Bull. Mineral.*, 1889, **12**(2), 36–38, DOI: **10.3406/bulmi.1889.2095**.

72 A. P. Laurie, W. F. P. McLintock, F. D. Miles and A. H. Church, *Proc. R. Soc. London, Ser. A*, 1914, **89**(612), 418–429, DOI: **10.1098/rspa.1914.0010**.

73 G. Schiappa and G. Torraca, *Bollettino Centralle di Restauro*, 1957, **31**, 91–107.

74 L. Goldberg, *J. Am. Inst. Conserv.*, 1996, **35**, 23–43, DOI: **10.1179/019713696806124601**.

75 S. Marcotte, L. Estel, S. Leboucher, S. Minchin and S. Le Meur, *Atmos. Pollut. Res.*, 2017, **8**, 483–489, DOI: **10.1016/j.apr.2016.12.002**.

76 C. Hawks, *Collection Forum*, 2001, **16**, 2–11.

77 P. J. Sirois and G. Sansoucy, *Collect. Forum*, 2001, **7**, 49–66.

78 A. I. Pfister, *La Lettre de l'OCIM*, 2009, 123, **http://journals.openedition.org/ocim/236**, DOI: **10.4000/ocim.236**.

79 G. Etesse, *Private Communication from Gaelle Etesse, Head of the Collection Department*, Musée-Chateau Comtal, Boulogne-sur-Mer, 2024, France.

80 A. M. Abdel-Karim, S. M. Zaid, M. I. Mohammed and M. G. Barakat, *J. Afr. Earth Sci.*, 2016, **123**, 10–20, DOI: **10.1016/j.jafrearsci.2016.07.005**.

81 M. F. Kaiser, A. M. Aziz and B. M. Ghieth, *J. Environ. Radioact.*, 2014, **137**, 7–78, DOI: **10.1016/j.jenvrad.2014.06.006**.

82 L. Beck, L. Pichon, B. Moignard, T. Guillou and P. Walter, *Nucl. Instrum. Methods Phys. Res., Sect. B*, 2011, **269**, 2999–3005, DOI: **10.1016/j.nimb.2011.04.059**.

83 V. Corregidor, J. L. Ruvalcaba-Sil, M. I. Prudêncio, M. I. Dias and L. C. Alves, *Materials*, 2024, **17**, 5075, DOI: **10.3390/ma17205075**.

84 M. Magalini, L. Guidorzi, A. Re, M. Marabotto, A. Borghi, P. Gallo, M. Vidale, L. La Torre, M. Campostrini, Q. Lemasson, L. Pichon, B. Moignard, C. Pacheco, P. Couture, V. Palitsin and A. Lo Giudice, *Eur. Phys. J. Plus*, 2025, **140**, 166, DOI: **10.1140/epjp/s13360-025-06095-5**.